Differential controls of forelimb versus whole-body movements by striatum

Jiaming Cao[1,3], Yujie Zhao[1,3], Jianing Yu[1,2,4,5]

[1] State Key Laboratory of Membrane Biology, Peking University, 100871, Beijing, China

[2] School of Life Sciences, Peking University, 100871, Beijing, China

[3] Academy for Advanced Interdisciplinary Studies, Peking University, 100871, Beijing, China

[4] IDG/McGovern Institute for Brain Research at Peking University, 100871, Beijing, China

[5] Correspondence: jianing.yu@gmail.com

Abstract

Neurons in the dorsolateral striatum (DLS) of the basal ganglia (BG) fire spikes that correlate with forelimb or whole-body movements during behavior, but their functional contributions remain debated. Using behavior-timed optogenetic inhibition in rats performing a lever-release reaction-time task, we found that transient DLS inhibition delayed the initiation of forelimb reaching and tone-cued lever release, and interrupted ongoing reaches. By contrast, it slowed whole-body locomotion during reward retrieval and reduced movement path efficiency, particularly during turns. Recordings from substantia nigra pars reticulata (SNr) showed bidirectional firing-rate changes during DLS inhibition, suggesting that altered BG output patterns mediate the behavioral effects. These findings indicate movement-type-specific DLS functions: the DLS facilitates and sustains forelimb initiation and execution while promoting efficient, rapid whole-body locomotion.

Introduction

Behavior has been defined as the total movement produced by the animal[1], within which learned movement sequences often involve repeated execution of actions with high precision, low variability, and rapid speed. Despite fine-scale dissections of the brain areas that may contribute to movement generation—including neural circuits in the cortex and basal ganglia[2–5], the roles of different neural structures in producing movements, and whether these roles generalize across movement types, remain unresolved[6,7]. The dorsal striatum, part of the BG, is widely implicated in the learning and execution of movements[8,9]. Indeed, striatal neural activity correlates strongly with behavioral events during procedural tasks and changes with learning[10–12]. However,

the precise functions of the dorsal striatum and the significance of its neural activity remain debated; proposals include action selection[13–15], encoding kinematic parameters of movements[16], controlling movement vigor (i.e., speed and force)[17–20], and storing or chunking motor sequences when behaviors become automatic[10,11,21]. In sum, striatal activity has been mapped extensively to movements, but how these signals contribute to generating and shaping movements remains unclear.

Discussions of BG models in movement control often overlook a critical factor: the specific movement types under study. Not all movements are equivalent. Eye movements involve only six extraocular muscles controlled by motoneurons in the oculomotor nucleus[22]. Forelimb reaching and lever manipulation involve more diverse upper-body muscle groups, including trapezius, deltoid, biceps, and triceps, controlled by motoneurons in the spinal cord[23–25]. Locomotion—including turning—depends on the coordinated activation of more diverse muscle groups across forelimbs, hindlimbs, trunk, and back[26–28]. Prior work has often focused either on precisely controlled forelimb movements[16,29–33], or on whole-body locomotion[18,20,33,34]. Whether the striatum contributes uniformly across movement types therefore requires systematic comparison.

We used a simple reaction time (SRT) task in which rats performed a tone-cued lever release to obtain reward[19,35,36]. The task required the rat to press and hold a lever before releasing it upon hearing a trigger tone. The reward (water) port on the opposite wall of the behavioral chamber required the rat to make a whole-body locomotor movement—including turning—followed by an operant nose-poke to obtain a water reward. Both forelimb and whole-body movements are learned operant responses, naturally chaining into a motor sequence. We implemented closed-loop, behavior-timed inhibition of the striatum to test its contributions[37,38]. First, we characterized how these movement types are represented in the DLS using chronic multi-site recordings (including Neuropixels probes). Second, by optogenetically activating inhibitory interneurons to suppress striatal projection neurons, we examined how closed-loop, behavior-coupled DLS inhibition affected movement initiation and execution. Finally, by recording from the output nucleus—the substantia nigra pars reticulata (SNr)—during DLS inhibition, we examined the firing properties in the SNr in the same task and linked the behavioral effects by DLS inhibition to changes in SNr neural activity. Our results demonstrate that the effects of DLS perturbations are movement-type-specific: forelimb movements are delayed or interrupted, whereas whole-body movements are slowed and less efficient. These effects are DLS-specific: inhibition of the dorsomedial striatum (DMS) had no effect on forelimb reaching and only mildly slowed whole-body movement.

Results

Event-locked DLS activity across SRT task phases

Rats were trained to perform a SRT task[19,35,36,39–41]. In a single session, the rat moved between a spring-loaded lever and a reward port in a custom behavioral box (Figure 1a). To start a trial (Figure 1b), the rat needed to voluntarily initiate a lever press, in the absence of any external cue, and hold it for an unpredictable duration (750 or 1500 ms), known as the foreperiod (FP). At the end of the FP, a brief, 0.25-s tone appeared and the rat released the lever within a 0.6-s response window to obtain reward. Premature or late responses were not rewarded. The reward port was located on the opposite side of the behavioral box, where water drops were triggered by a nose-poke following a correct lever release. Well-trained rats displayed stable, reactive lever releases across sessions (Figure 1c), exhibiting low premature responses and rapidly rising response probability right after the stimulus (Figure S1a). Rats formed stereotypical locomotor movement patterns in the operant box, traversing between the reward port and the lever (Figure 1d). Forelimb reaches were likewise stereotyped. After training, rats ($n=26$) made lever releases time-locked to the trigger tone (Figure S1a). The median correct response ratio was 68.8% (interquartile range(IQR): 65%–76.8%) for short FP trials (750 ms), and 63% (55.3%–67.4%) for long FP trials (1500 ms) (Figure S1b). The median reaction time was 0.34 s (IQR: 0.27–0.37 s) and 0.29 s (0.25–0.33 s) for short and long FP trials, respectively (Figure S1c).

We performed chronic multichannel recordings in the DLS of 10 rats using microwire arrays or silicon probes (including 2 rats implanted with Neuropixels probes; Figure 1e). Both wide (0.26 ± 0.07 ms, mean $\pm$ SD, $n=682$) and narrow (0.11 ± 0.05 ms, $n=123$) waveforms were encountered (Figure 1f–h). We focused our analysis on the wide-waveform units, representing putative spiny projection neurons (SPNs); remaining units likely originated from interneurons or *en passant* axons. Putative SPNs in the DLS had low average firing rates (median: 1.27 Hz; IQR: 0.68–2.46 Hz). After excluding units with extremely low firing rate even when modulated (maximal event-aligned spike density function (SDF) $<$ 4 Hz), non-significant task-related modulation (determined by a generalized linear model (GLM), Figure S2a; Equation 1, see Methods), or substantial inter-spike interval (ISI) violations ($>$ 2% of spikes had ISI $<$ 3 ms), we included 593 units for functional analysis, most of which ($n=563$) exhibited elevated firing during one or more task events (Figure 1k, l). During the SRT task, SPN activity was often modulated by one or more behavioral components (Figure 1i–l), including lever approach/press (example unit 1), lever holding (example units 2, 3), trigger/release (example units 1, 3, 4), and reward retrieval (example units 5, 6).

To capture modulation of population activity by behavior, we assembled a pseudopopulation using the soft-normalized average firing rate of 593 units and performed principal component analysis (PCA) (Methods). Firing rates were partitioned into two non-overlapping segments: (1)

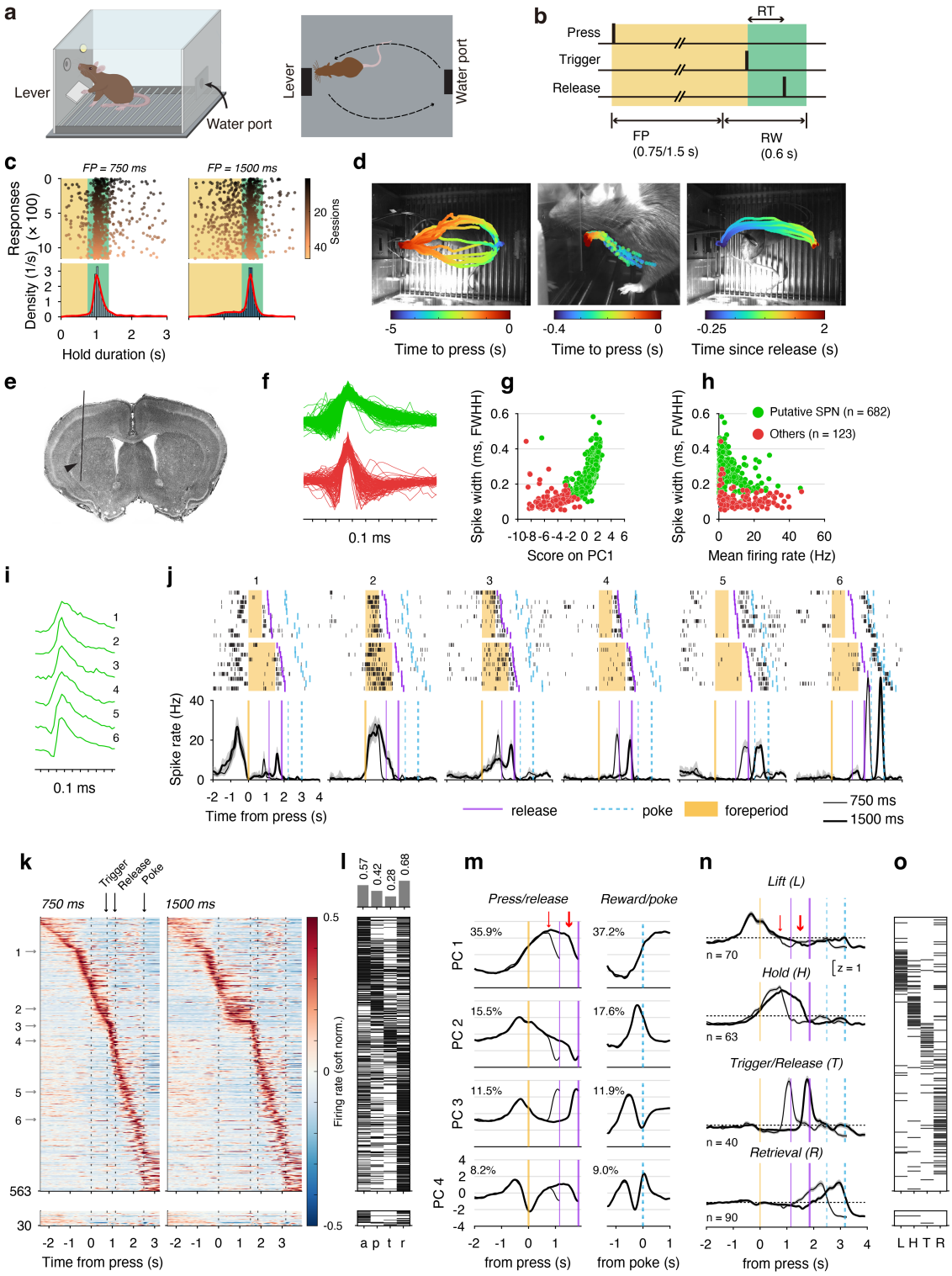

Figure 1. Simple reaction time (SRT) behavior and underlying dorsolateral striatum (DLS) neural dynamics. **a**, Behavioral apparatus schematic. **b**, Task structure (RT: reaction time; FP: foreperiod; RW: response window). **c**, Responses of a single rat across 47 sessions (25% of trials shown, colored by session index). Top: responses by occurrence time. Bottom: kernel density estimate (red). **d**, Movement trajectories of a single rat in one session. Left: lever approach (top view; frame size: 28×36 cm). Middle: paw reaching for lever presses (side view; frame size: 7×8 cm). Right: reward retrieval (top view). **e**, Example Neuropixels probe position in DLS. **f**, Two spike waveform types in DLS (amplitudes z-scored). **g**, Spike width (full width at half maximum, FWHM) plotted against projection onto the first principal component. Units classified via unsupervised clustering; green indicates putative spiny projection neurons.

Figure 1 (continued). **h**, Spike width plotted against average firing rate. **i**, Six example waveforms of putative spiny projection neurons. **j**, Spike rasters and spike density functions (SDFs) for example units in **i**. Rows 1–2: Rasters for 10 trials each of 750- and 1500-ms FP (yellow: FP; purple: lever release; cyan: nose-poke). Row 3: SDFs by FP type (thin/thick: 750/1500 ms; shading: 95% CI; purple/cyan: median release/poke times). All from one rat's Neuropixels data. **k**, SDFs of DLS units (rows: units; color: normalized rate). Top/bottom: positively/negatively modulated. Left/right: 750/1500 ms FP. Arrows mark examples from **i–j**. **l**, Modulation by approach (a), press (p), trigger (t) or retrieval (r) for each unit from a GLM (FDR $= 0.05$). Unit order is the same as in **k**. Histogram shows the proportion of units modulated by each event. **m**, Population projections onto the first four PCs around lever press (left) or port nose-poke (right). Thin/thick: 750/1500 ms FP. Colors match those in **j**. Numbers indicate variance explained. Red arrows: trigger onset. **n**, Average SDFs (z-scored) of functional units selected based on their projection loadings (see Methods). **o**, Index of selected functional units (Lift, Hold, Trigger/Release, or Retrieval); horizontal lines mark unit assignments, ordered from top to bottom to match the colormap order in **k**. Shading denotes SEM in **m** and **n**.

from lever approach (2.5 s before press) to lever release, and (2) from lever release to reward consumption (1 s after nose-poke). PCA subspaces were constructed separately for these periods. We projected population activity onto the top 4 PCs for visualization (Figure 1m), revealing that individual PCs often aligned with distinct behavioral features. The top 4 PCs captured 71.1% and 75.7% of the variance for the press/release activity and retrieval activity, respectively. Press/release subspaces reflected dynamics of lever approach and forepaw lifting (PCs 2, 3), holding (PCs 1–3), and release (PCs 1–4), while retrieval subspaces showed modulation peaking toward the nose-poke (PCs 1–3). Based on PC loading coefficients, we selected units with substantial contributions using *ad hoc* loading thresholds (Methods), which revealed average firing patterns tied to forepaw movements: lifting/lever press (L), holding (H), trigger/release (T), and reward retrieval movement (R) (Figure 1n,o, Figure S2b,c). There was small overlap among these units (Figure S2d). About 36.7% of retrieval units (33 out of 90) overlapped with forepaw-related units (Figure S2d). These results showed that distinct DLS neuron subsets are recruited across various behavioral phases, covering forelimb movements for the SRT task and whole-body movement for reward retrieval.

Using chronic Neuropixels probes, we observed sequential recruitment of DLS neurons aligned to task events in simultaneously recorded units during single sessions (Figure 2a). In an example session, a total of 84 type-1 units (putative SPNs) and 18 other units were recorded; of these, 64 type-1 units were modulated by behavioral events, a majority of which (57, 89.1%) were positively modulated. These units were modulated along the behavioral trial structure, with distinct behavior-relevant units intermixed along the dorsal-to-ventral axis in the striatum (Figure 2a). The neurons showed repeated phasic activation across trials (Figure 2b–d). After tracking the movement trajectories via DeepLabCut[42], we mapped spike rates onto the rat's movement trajectories to reveal the movement dependence of these task-modulated spikes (Figure 2e–g; see Methods, Equation 3). Some units (1 and 2) increased firing as the rat approached the lever, before lifting the forepaw; others fired during forelimb movements such as reaching (unit 3), lever press (unit 4), or lever release (units 5 and 6). Additional neurons increased firing during reward retrieval (units 7–10), which involved head turning toward the port. A similar pattern of activity was observed in another animal (Figure S3). Overall, DLS activity exhibited task-dependent sequential structure aligned to specific forelimb and whole-body movements across discrete SRT

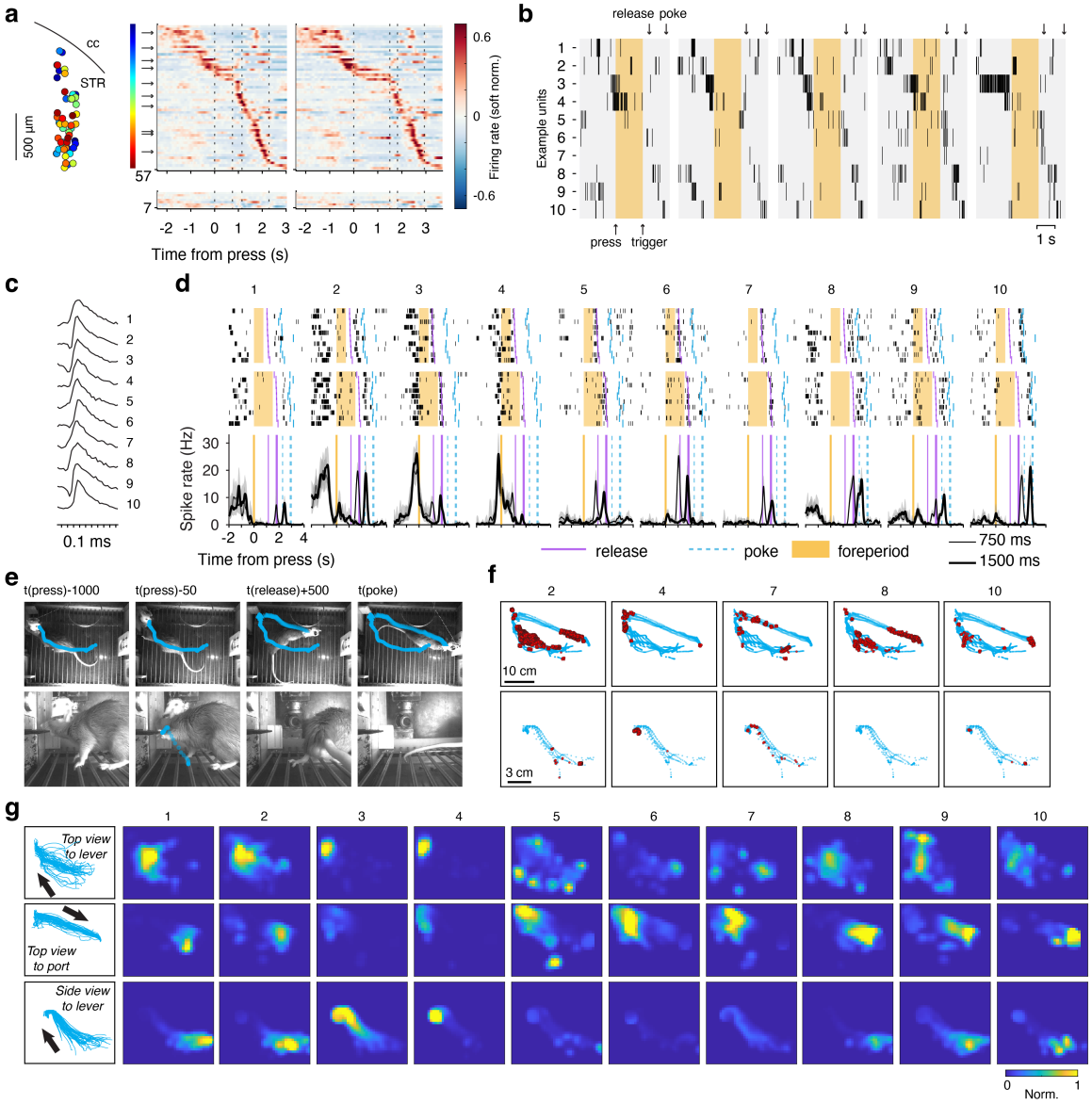

Figure 2. DLS neural activity tracks the rat's movements during behavior. **a**, Neuropixels recordings from a single session. Units (putative SPNs) are arranged as in Figure 1k. Arrows point to 10 example units; dorso-ventral locations of 57 positively modulated units are color-coded by their response timings. The dorsal boundary of striatum is shown (cc: corpus callosum; STR: striatum; relative to bregma: 0.68 mm). **b**, Spike rasters for 10 example units across 5 trials (FP = 1500 ms). Yellow rectangles denote the FP (press to trigger); arrows mark lever release and port nose-poke. **c–d**, Spike rasters and SDFs of the example units, as in Figure 1i–j. **e**, Representative frames at four time points: 1000 ms and 50 ms before lever press, 500 ms after release, and port nose-poke. Blue traces show head trajectories (first row, top view) or forepaw trajectories (second row, side view). **f**, Spikes (red) mapped onto trajectories for five example units. **g**, First column shows example movement trajectories. Other columns show spike rates mapped over space for 10 example units (each column is an unit). First row: head movement from lever approach to press; second row: head movement from trigger to port nose-poke; third row: forelimb movement during lever reach and press. Spike rates are color-coded and normalized to $r+c$, where r is the 0.99 quantile of each unit's spike-rate distribution and $c=1$.

phases—from lever approach to reward collection—consistent with the idea that task-related DLS spiking at least partly reflects low-level movement kinematics[16,43].

Optogenetic inhibition of striatum by activating interneurons

Striatum, like the cortex, contains local inhibitory interneurons controlling the flow of information through the circuits[44,45]. To probe the functional significance of task-related phasic activation of DLS neurons, we took advantage of an inhibitory interneuron-specific enhancer, mDlx, to introduce Channelrhodopsin-2 (ChR2) into striatal inhibitory interneurons[46,47] (Figure S4). Driving these interneurons temporarily inactivated SPNs with millisecond precision. Previous work has shown that the mDlx enhancer drives inhibitory interneuron-selective expression in the striatum with high fidelity[47]. After injecting a recombinant adeno-associated virus (rAAV) encoding mDlx and ChR2 into the DLS, co-labeling of neurons expressing Foxp1 (an SPN-specific marker) and neurons expressing GFP was low: 25 out of 1813 GFP+ neurons (1.4%) expressed Foxp1, while 2 out of 3526 Foxp1+ neurons (< 0.1%) expressed GFP (data from 2 rats, 18 slices). To validate this approach physiologically, we performed *in vivo* optrode electrophysiology recordings from 3 rats implanted with 16-channel opto-microwire arrays (Figure S4b). We performed electrophysiology recordings while rats performed the SRT task, and stimulated DLS with laser pulse trains (40 Hz, 5-ms pulse width, 2.2-s duration) randomly at different task phases, such as lever approach, with a low overall percentage (< 25% of all trials). Putative inhibitory interneuron units were activated by laser pulses, and their firing rates were elevated throughout the stimulation period (Figure S4c–e). Units with wide-waveform spikes were suppressed during stimulation and their behavior-related activation was reduced (Stim/NoStim spike rate ratio: median = 0.09, IQR: 0.03–0.32, $n = 96$ units with NoStim spike rate > 0.5 Hz; Figure S4f–j). Taken together, DLS photo-inhibition by driving DLS inhibitory interneurons produced sufficient inhibition of SPNs during behavior, allowing investigation of the effects of acute, behavior-coupled inhibition of the DLS.

Using this method, we combined closed-loop behavioral detection and optogenetics. For forelimb movements, we studied forelimb lift, lever press, lever holding, and lever release—critical components of a lever-press SRT task (Figures 3, 4, 5). For whole-body movements, we focused on the process of reward retrieval from lever release to nose-poke (Figure 6).

DLS inhibition delays forelimb reaching

To examine the effect of inhibiting the DLS on the initiation and execution of a lever press—a forelimb movement—we installed an infrared sensor above the lever. Once triggered, the sensor instructed the delivery of a 2.2-s, 40-Hz pulse train (each pulse: 5 ms) to the DLS in a small portion (10%) of trials (Figure 3a). As illustrated in the example, compared to uninhibited trials (NoStim), bilateral DLS photo-inhibition (PhotoInh) produced a delay in initiation of movement (Figure 3b,c,d; see Video S1). The press ratio—defined as the proportion of trials in which the rat pressed the lever within a 2.2-s window (duration of laser stimulation) following approach detection—decreased by 0.141 (median paired difference; 95% CI: $[0.1, 0.185]$; $p < 0.001$, Wilcoxon

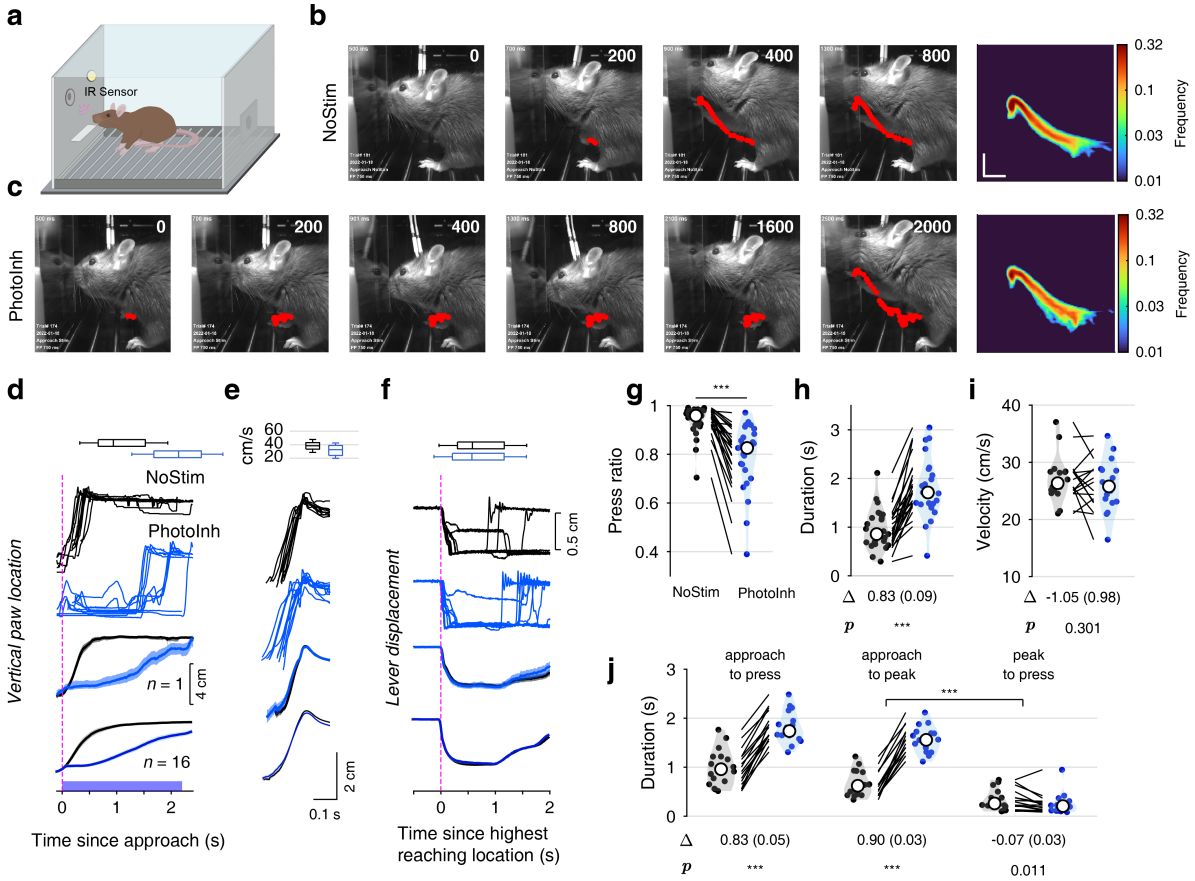

Figure 3. Bilateral DLS photo-inhibition delays the initiation of forelimb reaching. **a**, Schematic illustrating an infrared sensor detecting a rat's approach to the lever. **b**, Sequential video frames depicting a rat lifting its forepaw to press the lever. Frame numbers indicate time (ms) relative to approach detection (time = 0). Red dots trace the forepaw trajectory; the right-side heat map shows the across-trial frequency of forepaw crossings per grid square. Scale bar, 2.35 cm. **c**, Sequential frames of forelimb trajectory during bilateral DLS photo-inhibition (starting at time 0, duration 2.2 s). **d**, Top: horizontal box plots summarizing the distribution of approach-to-press durations across trials. Rows 1–2: example forepaw vertical positions from a single rat ($n=1$) for no-stimulation (NoStim; black) and DLS photo-inhibition (PhotoInh; blue) trials, aligned to approach detection. Row 3: average positions for the example rat (shading: 95% CI). Row 4: mean positions across 16 rats (shading: SEM). Blue rectangle denotes the laser stimulation period. **e**, As in **d**, but with forepaw vertical-position traces aligned to the time of the paw's peak vertical position; box plots summarize forepaw velocity during the lifting phase. **f**, As in **d**, but with lever-position traces aligned to the time of the paw's peak vertical position; box plots summarize durations from peak to lever press. **g**, Ratio of successful lever presses within a 2.2-s window following approach detection ($n=25$ rats). P-value from a two-sided Wilcoxon signed-rank test. **h**, Time from approach detection to lever press ($n=25$ rats). Values are estimated marginal means (EMMs, SEM in parentheses) for the PhotoInh−NoStim difference, derived from the LME model. **i**, Forepaw velocity during the lifting phase, as in **e** ($n=16$ rats). **j**, Time from approach detection to peak paw position and from peak position to lever press ($n=16$ rats). Values are EMMs for PhotoInh−NoStim differences within each duration type, derived from an LME model, with p-values adjusted using Holm's method. $***$ denotes $p<0.001$.

signed-rank test, two-sided, $n=25$ rats; Figure 3g).

We measured the duration from approach detection to the moment when the lever was pressed down (t_{a2p}) and fitted a linear mixed-effects (LME) model (Equation 4) that included stimulation type (StimType: NoStim or PhotoInh) as a fixed effect. The model also allowed random intercepts and random coefficient for StimType by rat to account for individual variability. Photo-inhibition

significantly increased t_{a2p} ($\beta_1 = 0.83 \pm 0.09$ s, mean ± SEM, $t(24) = 9.42$, $p < 0.001$, $n = 25$ rats; Figure 3h).

Lever-reaching trajectories during PhotoInh, when successfully initiated, did not differ from those during NoStim trials (Figure 3b,c,e). To evaluate the velocity of forepaw movement, in a subset of rats where the forepaw could be tracked without occlusion ($n = 16$), we fitted an LME model for velocity that included StimType as a fixed effect (Equation 5). The estimated marginal mean velocity was 27.07 ± 1.02 cm/s for NoStim (mean ± SEM), comparable to 26.02 ± 1.15 cm/s for PhotoInh. The coefficient (β_1) for StimType was -1.05 ± 0.98 cm/s ($t(14) = -1.07$, $p = 0.301$), suggesting a small and inconsistent population-level effect of DLS photo-inhibition on forepaw velocity.

Further, for each trial, we partitioned t_{a2p} into two parts, defining two duration types: from approach to lift peak (t_{a2pk}) and from lift peak to lever press (t_{pk2p}). We then fitted an LME model to study the interaction between the effect of photo-inhibition (StimType) and duration type (DurationType; Equation 6). There was a strong StimType × DurationType interaction ($\beta_3 = -0.97 \pm 0.02$ s, $t(8127) = -51.81$, $p < 0.001$, $n = 16$ rats), indicating that photo-inhibition affected these two durations differently. The increase in t_{a2p} (0.83 ± 0.05 s) was entirely attributable to the increase in t_{a2pk} (0.90 ± 0.03 s), but not the subsequent t_{pk2p} (-0.07 ± 0.03 s; Figure 3j). In addition, we monitored lever movement using a piezo sensor and reconstructed lever position (Figure 3f). Lever movements were indistinguishable for NoStim and PhotoInh trials (Figure 3f), suggesting a similar force was applied to the lever. Together, DLS photo-inhibition delayed forepaw lifting. However, once initiated during inhibition, forepaw reaching and subsequent lever press exhibited similar kinematics and vigor (velocity and force) between NoStim and PhotoInh conditions.

The results above were based on bilateral DLS photo-inhibition. In 10 rats, we examined the effect of unilateral photo-inhibition (contralateral or ipsilateral to the lever-pressing paw) on t_{a2p} and compared it with bilateral photo-inhibition (Equation 7, Figure S5a–e). Unilateral photo-inhibition also significantly decreased the press ratio and increased t_{a2p}. Overall, bilateral photo-inhibition had a stronger effect than contralateral inhibition, which was stronger than ipsilateral inhibition. These findings support a role for the DLS in initiating forelimb actions, suggesting that phasic pre-lift DLS activity contributes causally to initiation (e.g., example units 1–2 in Figure 2).

DLS inhibition interrupts execution of forelimb reaching

From the perspective of action selection[13,15], forelimb lever-reaching can be viewed as a single action selected from many alternatives, such as standing still, turning away, or using the contralateral paw. Once a lever-reaching movement was initiated, we asked whether DLS photo-inhibition modulated its execution. To our knowledge, this has not been tested for either forelimb or eye movements.

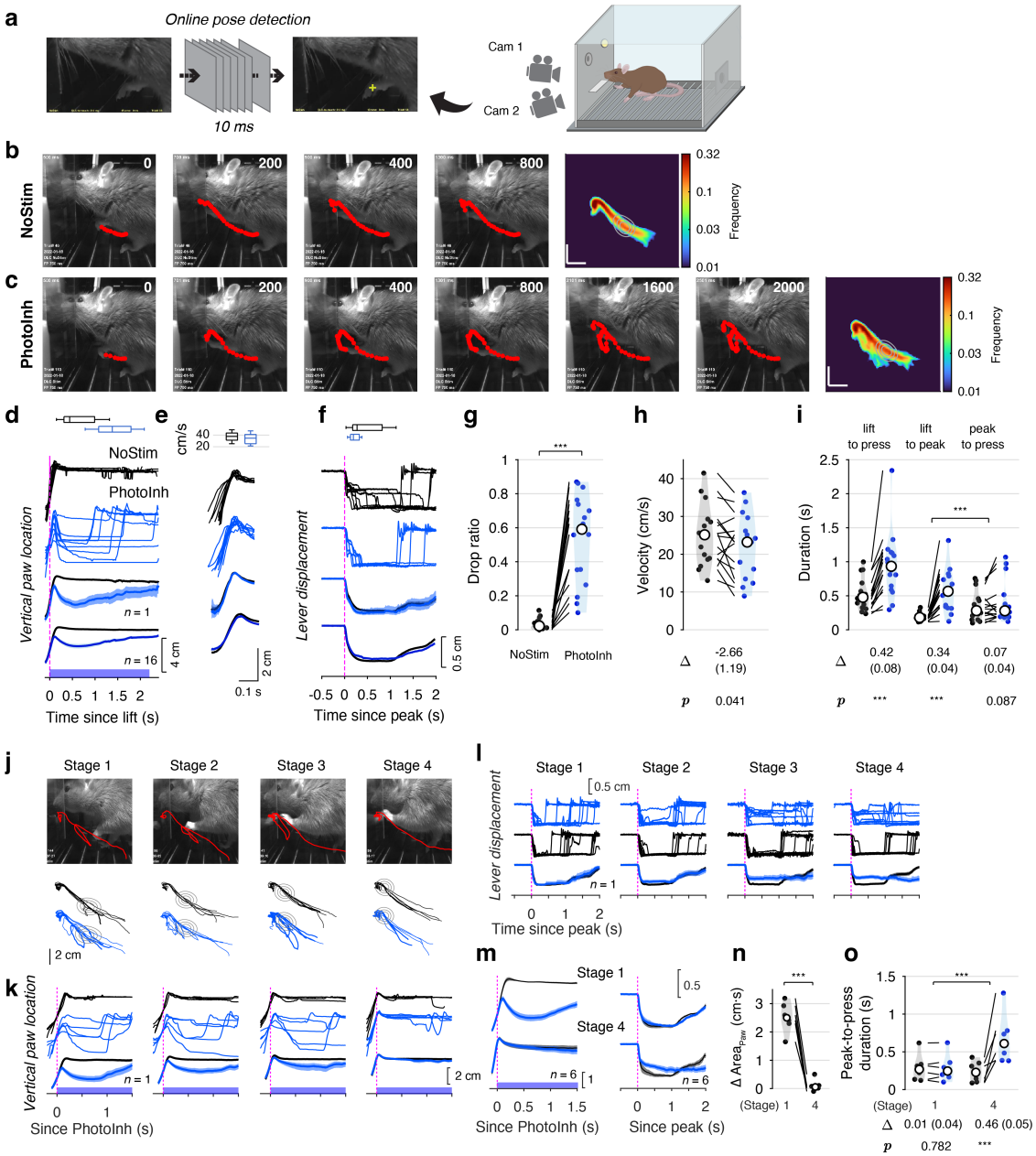

Figure 4. Bilateral DLS photo-inhibition interrupts the execution of forelimb reaching. **a**, Schematic illustrating online paw detection using a deep neural network. A dedicated camera captured frames in a small field of view at 50 fps; a second camera enabled high-speed video recording. **b**, Sequential video frames of a rat lifting its forepaw to press the lever. Frame numbers indicate time (ms) relative to lift detection (time = 0). Red dots trace forepaw trajectory; the right-side heat map shows forepaw crossing frequency per grid square across trials. **c**, Sequential frames of the forepaw trajectory during DLS photo-inhibition (2.2-s duration, starting at time = 0). **d–f**, As in Figure 3d–f, but with photo-inhibition applied at lift detection. **g**, Ratio of paw dropping within a 2.2-s window following lift detection. Black dots, NoStim; blue dots, PhotoInh; white circle, median; lines connect paired data from the same rat ($n = 16$). **h**, Forepaw velocity during the lifting phase ($n = 16$ rats). **i**, Durations from lift detection to peak paw position and from peak to lever press ($n = 16$ rats). **j**, Example frames showing four progressive stages of DLS photo-inhibition. Below each frame: example trajectories (black, NoStim; blue, PhotoInh); gray contours represent isodensity lines of paw positions across trials at the onset of PhotoInh. **k**, Paw vertical positions for each PhotoInh stage in the example rat from **j**. Time = 0 is PhotoInh onset. **l**, Lever positions for each PhotoInh stage in the example rat, aligned to the time of the paw's peak vertical position. **m**, Averaged paw vertical positions and lever positions from 6 rats across two PhotoInh stages. **n**, Integrals of differences in paw vertical position across two PhotoInh stages. P-value from paired t-test. **o**, Peak-to-press durations across two PhotoInh stages.

To achieve this, we implemented real-time, high-speed video-based pose detection with online estimation computed within 10 ms per frame at 50 Hz (Figure 4a)[48,49]. In a subset of trials (10%), paw lift triggered bilateral DLS photo-inhibition. Lift-triggered and approach-triggered photo-inhibitions were often interleaved within the same session.

As shown in the example, DLS photo-inhibition at lift onset interrupted reach execution, causing the paw to drop and hover for variable durations (Figure 4b–d; see Video S2). Paw-drop ratios increased by 0.499 (median paired difference; 95% CI: $[0.353,\ 0.683]$; $p<0.001$, Wilcoxon signed-rank test, two-sided, $n=16$ rats; Figure 4g). Rats often re-initiated reaching during PhotoInh (Figure 4c, d), with final trajectories and peak positions that were similar to NoStim (Figure 4e) but with a modest velocity reduction (10.6 ± 5.9% decrease; Figure 4h), likely due to mid-trajectory restarts. Despite these interruptions, following reaching restarts, subsequent lever pressing was not impaired (Figure 4f).

As above, we partitioned lift-to-press duration (t_{l2p}) into lift-to-lift-peak (t_{l2pk}) and lift-peak-to-press (t_{pk2p}) segments and fit a LME model (Equation 9). The model revealed a significant StimType × DurationType interaction ($\beta_3=-0.27\pm0.02$ s, mean ± SEM, $t(5444)=-12.55$, $p<0.001$), indicating that photo-inhibition affected the two durations differently. Photo-inhibition increased t_{l2p} (0.42 ± 0.08 s; Equation 8) primarily through a delay in t_{l2pk} (0.34 ± 0.04 s), with only a small effect on t_{pk2p} (0.07 ± 0.04 s)(Figure 4i).

We next designed an experiment to examine the effect of photo-inhibition along the reaching movement (Figure 4j). As the photo-inhibition onset was progressively delayed in the reaching movement, paw-drop rate reduced (Figure 4j–k) but lever pressing became more impaired (Figure 4l). In 6 rats, early-stage photo-inhibition altered forelimb trajectories (Figure 4m left, n), while late-stage photo-inhibition affected lever movements more strongly (Figure 4m right). LME modeling of t_{pk2p} (Equation 10) showed a StimType × Stage interaction ($\beta_3=0.45\pm0.04$ s, mean ± SEM, $t(967)=10.7$, $p<0.001$), confirming a larger effect on t_{pk2p} at later stage (0.46 ± 0.05 s) than at early-stage (0.01 ± 0.04 s) (Figure 4o). Together, these findings indicate time-sensitive DLS modulation of movement execution: the closer inhibition occurs to a movement's onset (immediately before or after), the larger the impairment on both initiation and execution.

The results above were based on bilateral DLS photo-inhibition. Compared with bilateral photo-inhibition, unilateral photo-inhibition produced weaker effects on paw-drop rate and on t_{l2p} (Equation 11, Figure S5f–j). Relative to the lifting paw, contralateral photo-inhibition had larger effect than ipsilateral photo-inhibition.

DLS inhibition prolongs reaction time

A prominent component of DLS neural dynamics was correlated with lever-release responses following the trigger stimulus (e.g., trigger-release units in Figure 1n and Figure S2B). To assess its functional role, we suppressed this activity by coupling laser onset to the trigger stimulus in rats

(Figure 5a) and examined the effects of DLS photo-inhibition on reaction time (lever release; see Video S3) and subsequent reward retrieval process (see below).

Trigger-coupled bilateral DLS photo-inhibition prolonged reaction times ($\beta_1 = 0.69 \pm 0.1$, mean ± SEM, $t(63.5) = 7.25$, $p < 0.001$, $n = 25$ rats; LME model in Equation 12), initially by 2.27-fold (750 ms FP) and 2.57-fold (1500 ms FP) (Figure 5d; Early Stim). This slowing effect attenuated with repeated inhibitions to 1.47-fold and 1.62-fold (Figure 5d; Late Stim), suggesting some degree of adaptation. Compared to bilateral DLS photo-inhibition, the effect of unilateral photo-inhibition was inconsistent (Figure S6). Overall, DLS activity coupled to trigger-release is crucial for initiating the forelimb lever-release responses.

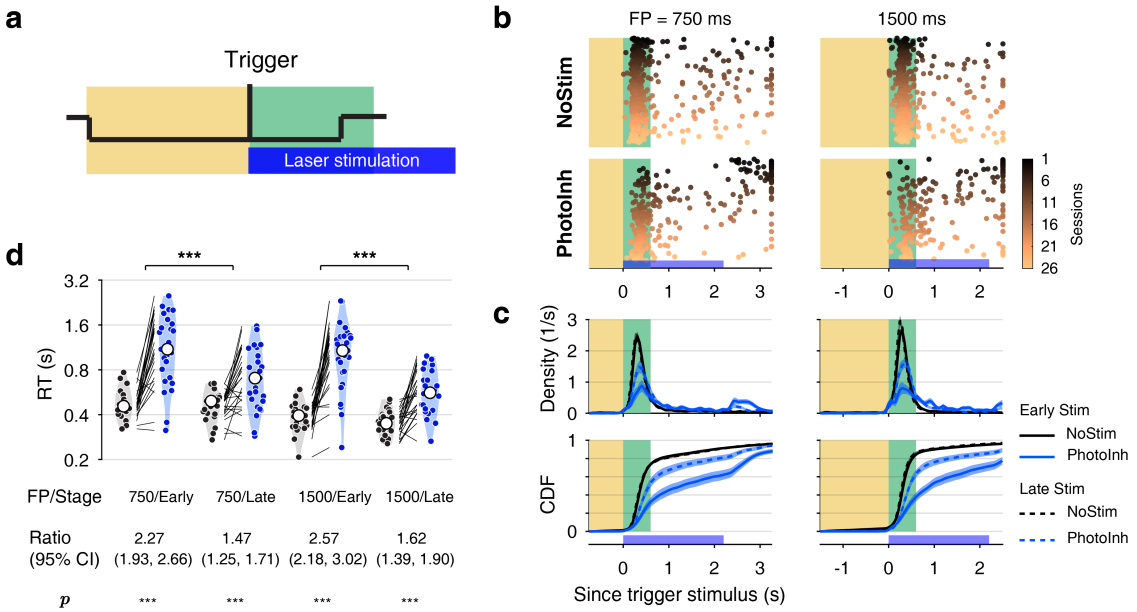

Figure 5. DLS photo-inhibition prolongs reaction time. **a**, Schematic of DLS photo-inhibition coupled to the trigger stimulus, applied only if no premature response occurred during the FP. **b**, Lever-release responses in an example rat with (blue) or without (gray; with 20% of trials plotted) bilateral DLS photo-inhibition, color-coded by session. Left: short FP (750 ms); right: long FP (1500 ms). **c**, Empirical probability density functions (PDFs) and cumulative distribution functions (CDFs) across $n = 25$ rats, with blue rectangle denoting laser stimulation. Solid lines: early photo-inhibition ($\leq$ 60 trials); dashed lines: late photo-inhibition ($>$ 60 trials); shading shows SEM. **d**, Geometric mean reaction times with (blue) or without (gray) trigger-coupled photo-inhibition across $n = 25$ rats, grouped by FP and photo-inhibition history (Early, Late). Violin plots show distributions; white circle, median; RT ratios (PhotoInh/NoStim), 95% confidence intervals (CI), and Holm-adjusted p-values from pairwise EMM contrasts from an LME model are displayed below.

DLS inhibition reduces locomotor efficiency and motor vigor during reward retrieval

In the behavioral box, following a correct lever release, rats retrieved water rewards from a reward port on the wall opposite the lever, requiring body turning, locomotion, and a self-initiated nose-poke (Figure 1a,d). Reward retrieval duration was defined as the time from lever release to nose-poke at the reward port. The retrieval duration did not influence reward size. To assess the impact of DLS photo-inhibition on the reward retrieval process, we coupled the

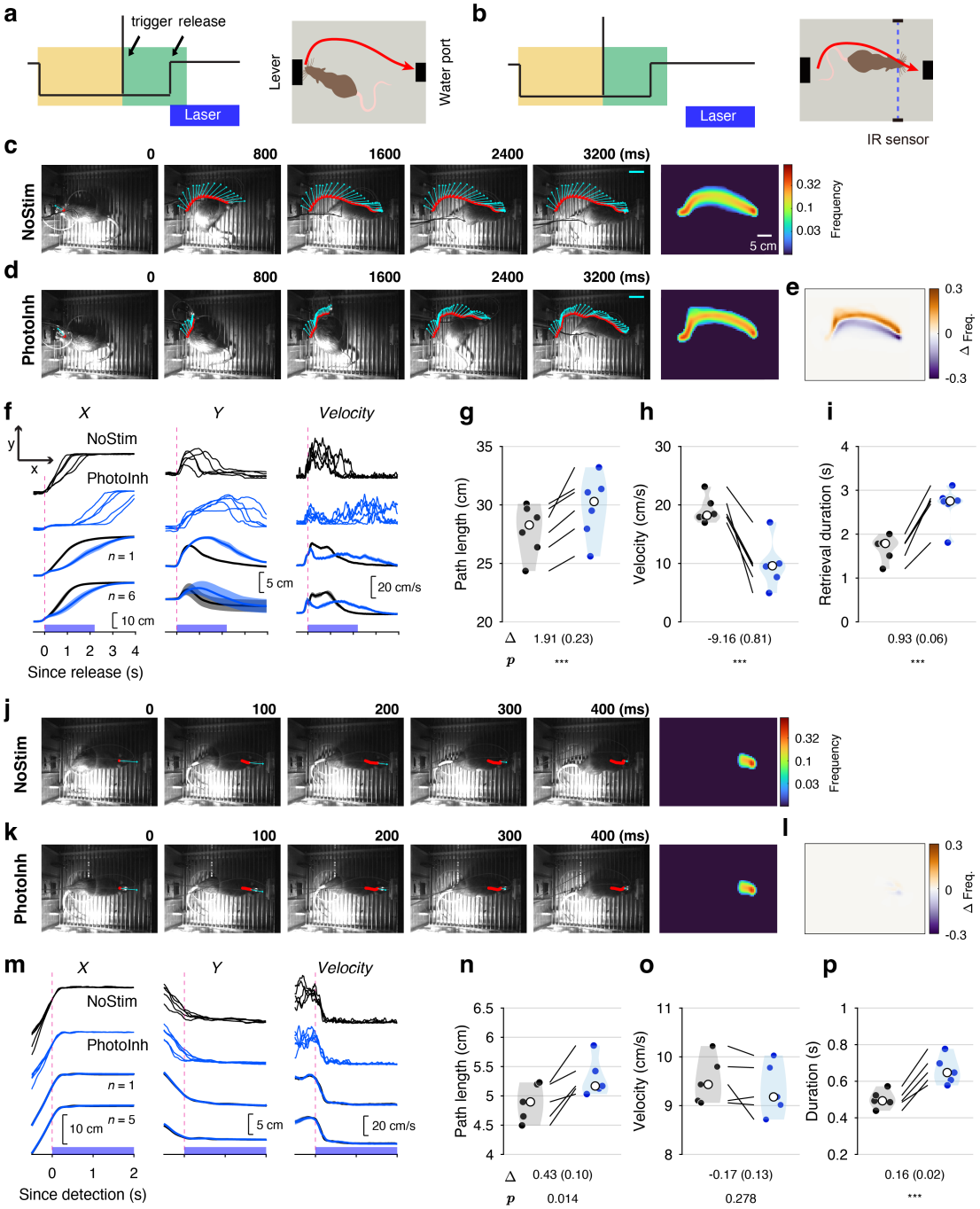

Figure 6. DLS photo-inhibition impairs whole-body movements during reward retrieval. **a**, Left: DLS photo-inhibition coupled to lever release. Right: Top-view camera tracks locomotion from lever release to port nose-poke. **b**, Left: Photo-inhibition coupled to an infrared sensor detecting the rat's approach to the water port. **c**, Frames at time points (ms) after lever release in a trial without photo-inhibition from a representative rat. Cyan arrows indicate head direction (50-ms intervals) with length denoting movement speed (scale bar, 20 cm/s); red dots mark head position. Right: trajectory heat map (color indicates pixel traversal frequency). **d**, As in **c** for a bilateral photo-inhibition trial (stimulation from time = 0). **e**, Difference in trajectory heat maps (**d** minus **c**). **f**, Movement along X (toward the water port) and Y, and instantaneous velocity. Rows 1–2: trials from the representative rat. Row 3: averages with 95% confidence intervals (shaded) for the representative rat ($n = 1$). Row 4: averages with SEM (shaded) across $n = 6$ rats. Blue rectangle indicates the laser-stimulation period. **g–i**, Movement path length, mean velocity, and retrieval duration for 6 rats (dots: individual-rat averages; circle: group medians). Mean differences (SEM in parentheses) and Holm-adjusted p-values are from pairwise EMM contrasts based on an LME model. **j–p**, Same as **c–i** for photo-inhibition near the water port, as illustrated in **b**.

onset of photo-inhibition to lever release (Figure 6a) and tracked head coordinates and direction using a top-view camera (Figure 6a).

Bilateral DLS photo-inhibition prolonged the reward retrieval durations, with trajectory frequency maps showing longer, more outward paths and reduced movement velocity (Figure 6d–f; see y position and velocity in Figure 6f). Movement nevertheless continued during photo-inhibition, without a full stop (see Video S4). Using an LME model with fixed effects including StimType (NoStim, PhotoInh) and StimSide (bilateral, ipsilateral, contralateral to turning direction) and random effects for animals ($n=6$; Equation 13), we found that bilateral photo-inhibition significantly increased path length ($\beta_1=1.91\pm0.23$ cm, $t(7.5)=8.34$, $p<0.001$), reduced velocity ($\beta_1=-9.16\pm0.81$ cm/s, $t(6.6)=-11.3$, $p<0.001$), and prolonged reward retrieval duration ($\beta_1=0.93\pm0.06$ s, $t(7.4)=15.28$, $p<0.001$), indicating impaired movement efficiency (larger outward turns) and reduced movement vigor (slower velocity). Compared to bilateral inhibition, unilateral inhibition showed similar but less pronounced effects, with ipsilateral inhibition producing larger effects than contralateral inhibition (Figure S7).

Note that when photo-inhibition was coupled to lever release, rats often had already begun moving toward the reward port (release and turn occurred nearly simultaneously). When DLS photo-inhibition was instead coupled to the trigger stimulus (Figure 5), despite longer reaction time, rats sometimes managed to release the lever within the response window, allowing us to test whether the subsequent reward retrieval process was affected (Figure S8; same example rat as in Figure 6c). The effects were similar: trigger-coupled DLS photo-inhibition also increased the reward retrieval duration, particularly with bilateral inhibition ($\beta_1=0.52\pm0.04$ s, $t(24.6)=12.42$, $p<0.001$, $n=25$ rats; Figure S8b,c). Movement tracking in a subset of rats ($n=11$; Figure S8d–j) demonstrated increased path length and reduced velocity, similar to Figure 6c–i (see Video S5).

We further examined the effects of DLS inhibition later in the retrieval movement. Using an infrared sensor near the reward port, bilateral photo-inhibition was applied toward the end of retrieval locomotion but before nose-poke ($n=5$ rats; Figure 6b; see Video S6). This occurred when rats began to decelerate (see velocity in Figure 6m) and prepared to make the next movement—the nose-poke. Photo-inhibition had little effect on the remaining trajectory (Figure 6j–m) and only slightly increased the path length leading to the nose-poke ($\beta_1=0.43\pm0.1$ cm, $t(4)=4.17$, $p=0.014$, Figure 6n). Photo-inhibition did not significantly change the movement velocity ($\beta_1=-0.17\pm0.13$ cm/s, $t(3.6)=-1.28$, $p=0.278$), suggesting that deceleration was normal. The duration from detection to nose-poke onset slightly increased ($\beta_1=0.16\pm0.02$ s, $t(4.6)=7.68$, $p<0.001$, Figure 6o–p). Overall, DLS photo-inhibition subtly delayed nose-poke behavior, contrasting with its much stronger effects on forelimb lifting during lever pressing (Figures 3 and 4).

Control and subdomain specificity

To minimize the visual confounds of laser stimulation, similar to previous optogenetics studies[50,51], all optogenetic experiments in this study were performed with a masking blue-LED flash (20 Hz, 4–6 s) mounted on the ceiling of the box, applied in both NoStim and PhotoInh trials and starting at lever approach. Furthermore, control experiments were performed in rats ($n=4$) injected with an AAV expressing GFP but lacking ChR2. Identical training, behavioral testing, and analyses were performed on these rats, and the results are shown in Figure S9. Briefly, in control rats, DLS photo-stimulation (i.e., sham photo-inhibition), when coupled to lever approach, did not change the approach-to-press duration (Figure S9a–e). It, however, slightly shortened reaction time when coupled to the trigger tone (Figure S9f–g), likely due to the additional visual cue provided by the laser coincident with the auditory tone. DLS photo-stimulation had no effect on whole-body locomotor movement toward the reward port (Figure S9h–n). Thus, our observed behavioral effects of DLS photo-inhibition were attributable to modulation DLS and downstream activity, rather than other factors, including tissue heating[52].

In addition, we performed parallel experiments and analyses in the dorsomedial striatum (DMS) using the same methods and pipeline ($n=12$ rats; Figure S10a-b). DMS photo-inhibition produced no detectable change in the approach-to-press duration, that is, forelimb movement initiation was not impaired (Figure S10c–i). We did not perform additional lift-coupled photo-inhibition. When photo-inhibition was coupled to lever release, we observed a slowing of whole-body movement velocity and an increase in reward retrieval duration, but the effect was substantially smaller than with DLS photo-inhibition (Figure S10j–p). Taken together, both lateral (DLS) and medial (DMS) domains of the dorsal striatum contribute to whole-body movement vigor, whereas DLS also gates and controls forelimb reach initiation and execution.

DLS inhibition results in mixed responses in BG output (SNr)

The behavioral effects of striatal photo-inhibition ultimately manifest as changes in BG output through structures such as the SNr[53,54], with further downstream effects on structures including the motor thalamus, superior colliculus, and brainstem[55–59]. Increasing BG output inhibits downstream circuits, delaying forelimb movement inhibition[55] or suppressing repetitive licking[60]. Decreasing BG output has been shown to slow reaching movements in monkeys[30]. Thus, perturbing BG output in either direction potentially can impair movement.

To examine the consequences of DLS inhibition on BG output in our task, we conducted tetrode recordings from the SNr of 9 rats during SRT task. In 6 of these rats, we bilaterally implanted optical fibers in the DLS, enabling simultaneous SNr recordings during DLS photo-inhibition (Figure 7a). Spike waveforms recorded in the SNr showed a continuum of widths and shapes, which we roughly grouped into two types (1 and 2) by examining spike width (type 1: 0.1 ± 0.02 ms, $n=249$; type 2: 0.18 ± 0.03 ms, $n=64$; mean $\pm$ SD) and principal component (Figure 7b,c).

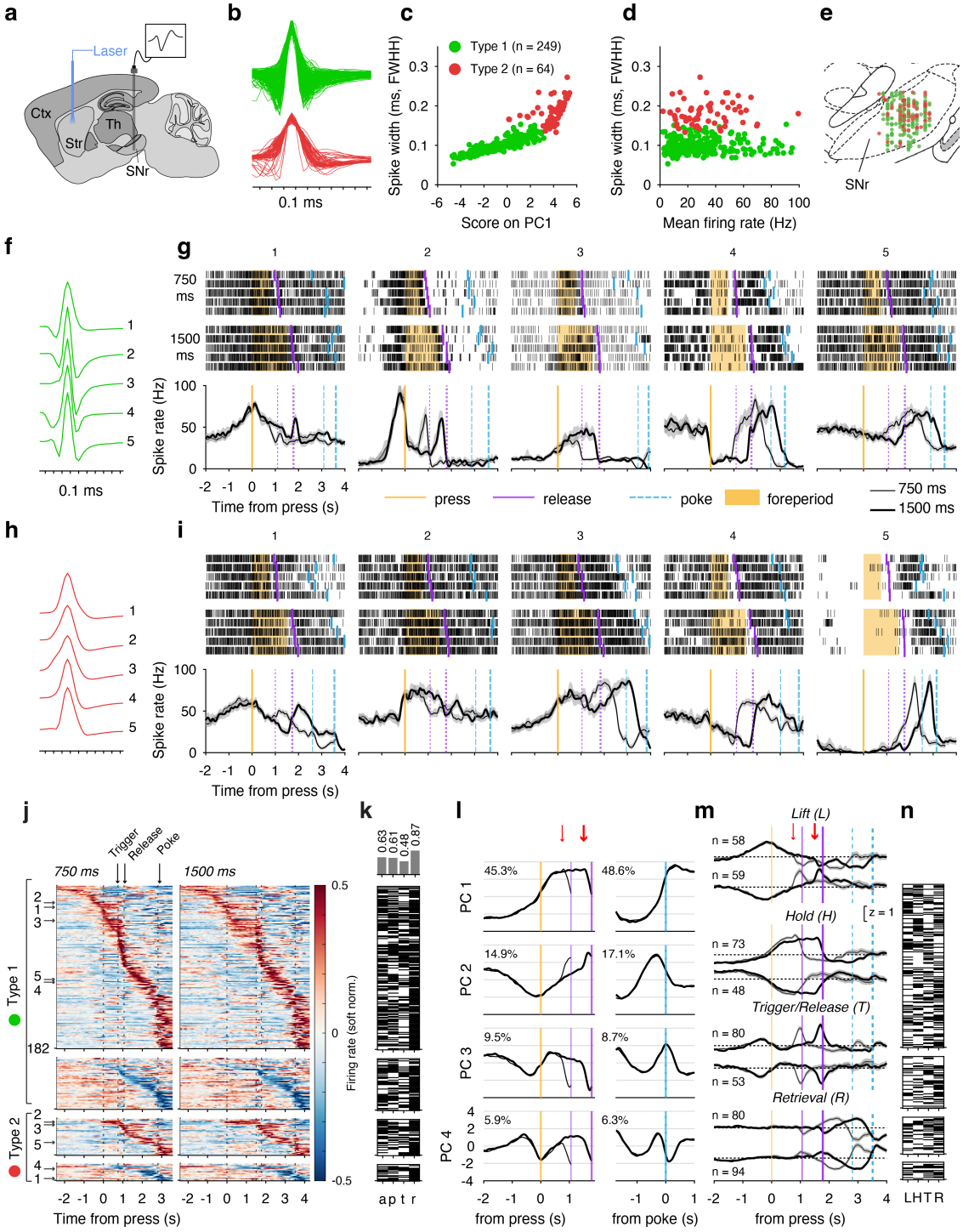

Figure 7. Neural activity in the substantia nigra pars reticulata (SNr) during the SRT task. **a**, Schematic of tetrode recordings, often combined with striatal photo-inhibition. **b**, Two waveform types (1 and 2) recorded in the SNr with different widths; waveforms are shown with negative voltage upward. **c**, Spike width (FWHM) plotted against projection onto the first principal component. **d**, Spike width (FWHM) plotted against average firing rate. **e**, Estimated locations of these units in the SNr. **f**, Five example type-1 unit waveforms. **g**, Spike rasters and SDFs for the example units in **f**. Same layout as Figure 1i. **h–i**, Same as **f–g** for five example type-2 units. **j**, SDFs (soft-normalized) of SNr units: rows 1–2 show positively and negatively modulated type-1 units; rows 3–4 show type-2 units. **k**, Modulation by event for each unit from a GLM (FDR = 0.05). Unit order is the same as in **j**. Histogram shows the proportion of units modulated by each event.

Figure 7 (continued). l, Population projections onto the first four PCs around lever press (left) or port nose-poke (right). Thin/thick: 750/1500 ms FP. Colors match those in **j**; numbers indicate variance explained. Red arrows: trigger onset. **m**, Average SDFs (z-scored) of functional units selected based on their projection loadings (see Methods). **n**, Index of selected functional units (Lift, Hold, Trigger/Release, or Retrieval); horizontal lines mark unit assignments, ordered from top to bottom to match the colormap order in **j**. Shading denotes SEM in **l** and **m**.

These unit types were spatially intermixed across depths and showed similar baseline firing rates (Figure 7d,e), possibly corresponding to genetically defined cell types such as parvalbumin (PV) and non-PV neurons[56,61] or those projecting to specific targets[57]. Using the same criteria as for DLS units, including ISI violations and event modulation, we selected 240 (type 1) and 60 (type 2) SNr units for further analysis.

Consistent with prior work[31,55,62,63], SNr neurons showed heterogeneous firing patterns during behavior, with behavior-relevant increases or decreases in firing rate from a high baseline, modulated by events such as lever approach, press, holding, release, and reward retrieval (Figure 7f–k). Both type-1 (thin waveform) and type-2 (wide waveform) SNr neurons were modulated. PCA identified subspaces capturing variance in population activity modulated by forelimb responses or reward retrieval, with SNr population projections similar to those in DLS (Figure 7l). As before (Figure 1n), these PCA subspaces guided selection of units based on their loadings (Figure 7m, n). Notably, selectivity was more mixed for SNr units (Figure 7k,n; Figure S2g): 85.6% of retrieval units overlapped with lift/hold/trigger units in SNr, a greater proportion than for DLS units (36.7%, Figure S2d; $\chi^2(1,1)=61.2$, $p<0.001$, chi-square test). These results suggest convergence of behavior-relevant modulation from DLS to SNr.

In a subset of SNr recordings ($n=124$ units), press-aligned DLS photo-inhibition was collected in a small percentage of trials. We aligned activity to lever press because, although premature responses increased with DLS photo-inhibition, they typically emerged only after repeated stimulation and increased with longer holding durations, not immediately after the press (Figure S11). We selected trials for which the holding duration was at least 500 ms for both NoStim and PhotoInh conditions, so that the first 500 ms of behavior was matched across conditions, allowing us to compare neural activity directly (Figure 8a–d). As demonstrated by these examples, the effect of DLS photo-inhibition on single SNr neurons could either be an increase or a decrease in firing rate (Figure 8e–f) and the distribution of change direction was not different between type-1 and 2 neurons ($\chi^2(2)=0.22$, $p=0.895$, chi-square test; Figure 8g). The change occurred around 14 ms (time at half maximum) for firing-rate decreasing neurons and 8 ms for firing-rate increasing neurons (Figure 8f). The complex effect of DLS inhibition on SNr neurons observed here is consistent with prior work using striatal activation or inactivation[53,54].

There was a significant negative correlation between the firing rate (FR) in the NoStim condition and the modulation magnitude ($\mathrm{FR}_{\mathrm{PhotoInh}}-\mathrm{FR}_{\mathrm{NoStim}}$) under photo-inhibition (Spearman's $\rho=-0.43$, d.f.$=122$, $p<0.001$), indicating that neurons with higher baseline firing rates tended to show reduced activity during DLS photo-inhibition, whereas those with lower firing rates tended

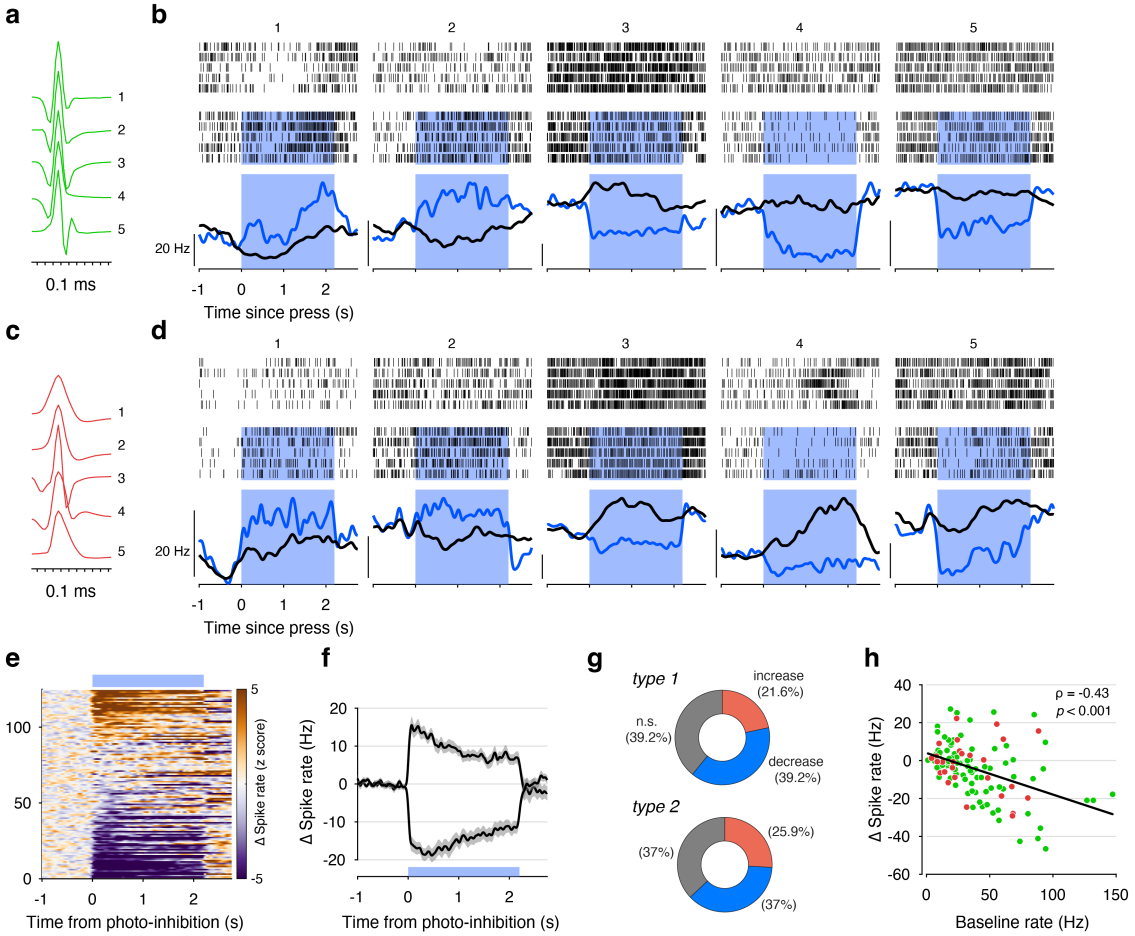

Figure 8. DLS photo-inhibition bidirectionally modulates SNr neuron spike rates. **a**, Example waveforms of five type-1 SNr neurons. **b**, Spike rasters and SDFs (black, NoStim; blue, Photo-inhibition) for five example type-1 SNr neurons with and without DLS photo-inhibition, aligned to lever-press onset. Blue rectangles indicate laser stimulation periods. **c–d**, Same as **a–b** for five type-2 SNr neurons with wider waveforms. **e**, z-scored SDFs of 124 neurons(PhotoInh−NoStim), ordered by firing-rate changes during photo-inhibition, from increased firing (top) to decreased firing (bottom). **f**, Mean SDFs of 28 neurons with increased firing rates versus 28 neurons with decreased firing rates during photo-inhibition. **g**, Distribution of type-1 and type-2 neurons showing increased or decreased firing rates during DLS photo-inhibition. **h**, A negative correlation between baseline (NoStim) firing rate and the change in firing rate due to DLS photo-inhibition.

to show increased activity (Figure 8h).

Discussion

The roles of the basal ganglia (BG) in movement control have long been debated[17]: whether they shape movement kinematics[16], select among competing actions[13,15], or invigorate the chosen movement[18,29,64]. However, whether these functions are linked to specific movement types has received less attention. We used optogenetic inhibition of the DLS in a lever-release reaction-time task to test whether striatal inhibition differentially affects movement types. DLS inhibition

impaired forelimb and whole-body locomotor movements differently: it delayed forelimb movement initiation—including reaching and lever release—and disrupted execution, whereas whole-body locomotion was slowed continuously throughout the inhibition period, without a complete pause, and followed less efficient trajectories. Together, these findings indicate that the DLS supports the initiation and execution of forelimb movements, while regulating velocity and path efficiency during whole-body locomotor movements. By contrast, the neighboring subdomain, DMS, contributed to whole-body locomotion but had no detectable effect on forelimb reaching movements.

Neural activity in DLS and SNr is linked to diverse movement types

In our experiment, the lever and the reward port were placed on opposite sides (32 or 35 cm apart) of a behavioral box, naturally segregating lever-related forelimb movements from reward-oriented whole-body locomotion. Individual DLS neurons were selectively coupled to one or more discrete behavioral events such as lever approach, paw lift (reach), lever press and hold, lever release, and reward retrieval. Neural activity was also modulated by these events in the BG output nucleus, SNr. Comparing the activity patterns, using either event-modulation or PCA-based unit selection, revealed more mixed selectivity in the SNr (e.g., compare Figure 1l,o and Figure 7k,n). That is, a single SNr neuron is more likely to be modulated at multiple event points in a task, linked to several movement types.

Photo-inhibition of DLS neurons produced mixed effects in the SNr: some neurons increased their firing rate and others decreased firing rate, consistent with other work[53,54]. The firing rate of an SNr neuron is determined by many factors, including its intrinsic firing properties independent of synaptic inputs[57], inhibitory input from direct and indirect pathways, and excitatory input from the subthalamic nucleus (STN)[65,66]. Although the precise rules of connectivity from striatum to SNr remain largely unexplored, our results suggest that information from multiple striatal inputs converges onto single SNr neurons, producing multiplexed firing patterns. Withdrawal of striatal input disrupted the normal firing patterns of SNr neurons, which impaired movement. Indeed, abnormal output patterns in BG are thought to be the cause of striatum-related disorders such as Parkinson's disease[67].

Differential effects on forelimb and locomotor movements by DLS inhibition

DLS photo-inhibition had distinct effects on forelimb versus whole-body locomotor movements. When applied before movement onset, forelimb reaching or tone-cued lever release was delayed, consistent with an action-selection role[15,68]. After reach initiation, DLS photo-inhibition interrupted ongoing execution, indicating that the DLS also contributes to the progression of an initiated movement. Notably, in both cases, reaches were often re-initiated during inhibition and completed at similar velocities and along similar trajectories as in uninhibited trials, suggesting

that, under the current experimental conditions, DLS activity is neither required for producing these movements nor critical for determining the reaching velocity in the air.

Our previous lesion study showed that DLS-lesioned rats moved more slowly and made larger circles when turning toward the reward port[19], a pattern recapitulated by DLS photo-inhibition. Unlike forelimb movements, whole-body locomotion did not stop completely with photo-inhibition: rats continued toward the reward port at lower speed and via larger circles, indicating degraded movement vigor (defined as "speed, amplitude, or frequency" of a movement[17]). Nose-poking into the reward port was largely preserved during DLS photo-inhibition, in sharp contrast to lever pressing, despite both actions being movement initiations involving interaction with an operandum.

Distinct neural mechanisms may underlie isolated forelimb versus whole-body movements. A classic example comes from bilateral corticospinal tract lesions in monkeys[6], where in the days after surgery, distal limb movement (e.g., food grasping) was more severely impaired than whole-body movements such as walking and climbing.

Comparisons with previous work

In head-fixed mice, striatal inactivation with archaerhodopsin-3 (ArchT) during joystick movement reduced movement velocity while leaving displacement unchanged[29]. This observation can be compared to our experiment when DLS photo-inhibition was applied during forepaw lift, in which animals dropped the paw mid-air and then re-initiated the reaching movement moments later, yielding reduced velocity to complete the same displacement (Figure 4h). Notably, paw dropping was not reported in the joystick task, possibly because the joystick prevented dropping by acting as a support.

Studies using lever-press tasks have observations supporting forelimb initiation deficits with DLS inhibition. In a study where striatal inactivation by ArchT was coupled to lever approach, the duration from approach to lever press lengthened, suggesting initiation impairment for lever press[33]. Similarly, halorhodopsin-mediated DLS inhibition increased completion time on a fixed-ratio (FR-3) task when rats were trained to make multiple presses to earn a reward, which was likely due to initiation difficulty as inter-press intervals increased[69]. In our work, we observed an increase in approach-to-press duration and quantitatively analyzed the forepaw movement, pinpointing that the increased duration was caused by a delay in lift initiation, not a general slowing of forelimb movement during lever reaching or difficulty pressing the lever (Figure 3j). In addition, we coupled the inhibition to ongoing reaching by online pose tracking, further testing whether DLS is also required for completing initiated movement (Figure 4), which to our knowledge had not been conducted previously.

Other prior work has pointed to reduced whole-body movement vigor with striatal inhibition. For example, when rats were trained to perform a decision-making task in a T-maze, DLS

inhibition by halorhodopsin increased trial duration[70]. In another study, an increase in "choice time" was observed following inhibition of direct-pathway SPNs of mice performing an interval-categorization task[38]. "Choice time" was defined as the movement time from a central port to a side port that delivers reward when selected correctly. Hence, its increase suggests a reduction in whole-body movement vigor, consistent with our finding during reward retrieval (Figure 6). In another study[33], unilateral DLS inhibition was shown to reduce contraversive turning and bias animals toward ipsiversive turns. However, we found that unilateral DLS photo-inhibition slowed reward-retrieval locomotion, with inhibition in the side ipsilateral to the turning movement producing a larger effect than contralateral inhibition (Figure S7). A direct comparison is difficult, because spontaneous turning and reward-oriented retrieval differ in task demands and kinematics.

In monkeys performing a center-out task, chemical inactivation of the BG output nucleus, the globus pallidus internus (GPi), slowed forelimb movement velocity but preserved other kinematic features, including trajectory and habit-like features[30,71]. In this task, the monkeys used a joystick to track a target. Together with related work (see references in[64]), this constitutes strong evidence supporting the vigor hypothesis over alternatives, such as action selection or skill retention. In our experiments, once forelimb reaching was re-initiated under photo-inhibition, despite a delay, its trajectory and velocity were similar to uninhibited trials (Figure 3d,e,f), and the subsequent lever press was also normal, indicating no detectable reduction in forelimb movement vigor. Several factors may account for differences across paradigms: First, moving an object (e.g., a joystick), which provides constant somatosensory feedback and support, may engage the BG differently than free-air reaching. Second, perturbing the BG output may produce different behavioral effects than perturbing the input. DLS photo-inhibition caused bidirectional SNr responses (Figure 8), whereas muscimol inactivation abolishes all GPi activity. Third, sustained inactivation, including chemical inactivation or lesion, may produce different behavioral effects compared to transient optogenetic inhibition delivered in a small fraction of trials[72,73]. Indeed, bilateral DLS lesions in the same task resulted in reduced forelimb reaching velocity even following extensive post-operative training[19]. However, bilateral DLS lesions persistently impaired behavioral performance in the SRT task, reduced reward rate, and altered movement trajectories[19], which may contribute to slower forelimb movement. Taken together, the neural substrates that determine forelimb reaching velocity in rodents remain unclear. Our data indicate that DLS inhibition does not abolish a reach but instead transiently delays or interrupts it; thus, vigor-based models are insufficient on their own to explain these forelimb findings.

Limitations

Rats are well suited for reaction-time experiments: their forelimb and whole-body movements are quantifiable in freely moving paradigms, their lever-press behaviors are stereotypical once stabilized, and their size accommodates large implants with minimal impact on behavioral

performance. However, our approach—driving inhibitory interneurons to suppress the firing rate of projection neurons[46,74]—does not isolate cell-type- or pathway-specific effects: both direct (striatonigral) and indirect (striatopallidal) pathways are suppressed. Future work could leverage transgenic rats[75] or molecular tools[76] to selectively perturb these pathways. Alternatively, one could target downstream circuits directly, including the external globus pallidus (GPe)[77] or silence DLS outputs using axonal-silencing approaches[66]. That said, the current approach and its variants (e.g., activating striatal PV-positive interneurons) produce robust suppression of SPN spiking, functionally akin to a precisely timed lesion, and can motivate more fine-scale perturbations. Moreover, pathway-specific manipulations are often complicated by lateral interactions: increasing or decreasing the activity of one cell type inevitably changes the activity of the other[44,77].

During the reward retrieval phase, rats made a turning motion toward the reward port. DLS photo-inhibition markedly slowed this process and altered the movement trajectory (Figure 6d). One possibility is that turning, relative to straight-line locomotion, relies more heavily on the DLS, which could account for much of the whole-body slowing. Turning indeed is strongly represented in the DLS (e.g., unit 7 in Figure 2, unit 7 in Figure S3; see also[12,34]). However, our behavioral box was not large enough to fully assay straight-line locomotion—rats typically reached the reward port shortly after the turn and began to decelerate. Future experiments in a maze (e.g., a T-maze[10,70,78]) combining turning with straight-line locomotion in a long corridor could directly investigate this question.

Conclusion

Together, our data show that the behavioral effects of DLS photo-inhibition depend on movement types, an often overlooked factor. BG models should account for the fact that different movements require distinct muscle sets, magnitudes, and coordination. Accordingly, the role that DLS plays may vary across movement types.

Methods

Animals

All animal procedures were conducted in accordance with the animal care standards set forth by the US National Institutes of Health and were approved by the Institutional Animal Care and Use Committee of Peking University. Male adult Brown-Norway rats were obtained from Vita River Laboratories (Beijing, China). Rats were older than three-month old and weighed 250–400 g prior to water restriction and behavioral training. Rats were housed individually on a 12-hour reverse light-dark cycle. During water restriction, water was earned during behavioral sessions; if intake was less than 12 mL, supplemental water was provided at least 3 hours after the session. Rats' body weights were maintained at approximately 80% of their free-feeding level. Training was conducted 6 days per week, with unrestricted water access on the seventh day.

Apparatus and Behavioral training

Behavioral training protocols were detailed in a prior study[19]. Briefly, custom operant chambers integrated lever-based response modules (Med Associates, Fairfax, VT, USA) with Bpod state machines (Sanworks LLC, Rochester, NY, USA) for precise control of reward delivery and event timing. Within each chamber, a retractable response lever and reward port were positioned on opposite walls, separated by 32 cm (optogenetics experiments) or 35 cm (Neuropixels recordings). Behavioral programs were written in MedState Notation (MSN) by Marcelo Caetano and Mark Laubach. SRT behavioral performance was shaped progressively across six stages: (1) autoshaping; (2) lever press; (3) lever release; (4) lever hold (FP: 0 increased to 1.5 s) with a wide release response window (2 s); (5) hold with rapid release incentives (response window: 2 reduced to 0.6 s); and (6) full SRT schedule (0.75, 1.5 s FP, 0.6 s response window). The lever remained extended throughout sessions (except for autoshaping), with trials self-initiated by lever presses. Correct responses triggered illumination of an LED within the reward port, cueing delivery of a 60-μL, 10% (w/v) sucrose solution upon nose-poke entry. Error responses (premature or late release) were penalized by a timeout (4–10 s) with the lever light and house light turned off (lever not retracted). The imperative trigger stimulus was a 250-ms tone (2 kHz, 70 dB SPL) delivered via a speaker mounted above the lever. An infrared LED, synchronized to tone onset, provided a signal for aligning video timestamps with behavioral events. A side-view camera (MER-160-227U3M, Daheng Imaging, Beijing, China, 100 fps) was positioned externally to record lever-press forelimb kinematics. An overhead camera (MER-160-227U3M, 100 Hz) captured top-view images of locomotor behavior.

In closed-loop optogenetic experiments, a transparent acrylic plastic block was placed directly in front of the lever to constrain rats' movement angle and posture, facilitating detection of

lever-approach and paw-lifting behaviors. A 40-cm rectangular gap allowed access for lever pressing, thereby abolishing presses from extreme side angles.

Stereotaxic surgery

Prior to surgery, rats were given unrestricted access to water for at least 2 days. Animals were anesthetized with isoflurane (induction: 4%; maintenance: 1–2% in O_2) and mounted in a stereotaxic frame (MTM-3; World Precision Instruments). Rectal temperature was maintained at 37.5°C via a feedback-controlled heating pad. Eyes were lubricated with erythromycin eye ointment (Qilu Pharmaceutical, Jinan, China). Fur was removed using an electric clipper, and the scalp was sterilized with iodine tincture followed by 75% ethanol (3×). The scalp was incised along the midline, and the pericranium was reflected using a blunt scalpel. The skull surface was further cleaned with 3% hydrogen peroxide. Craniotomies were drilled at the target coordinates, and the dura was carefully incised using a 30-gauge needle prior to injection or implantation.

Virus injection

Virus injections and optical fiber implantation (described below) were conducted on separate days. Injections were performed using glass pipettes (Drummond Wiretrol II, Broomall, PA, USA) mounted on a custom-made injector system (Stereotaxic Injector System, Janelia) or a motorized microsyringe pump (UMP3; World Precision Instruments) coupled to a 10-μL precision syringe (701 RN; Hamilton, Reno, NV, USA) fitted with a removable needle (Hamilton; 33 gauge, 12 mm). AAV2/9-mDlx-hChR2(H134R)-EGFP-WPRE-pA or a control virus AAV2/9-mDlx-EGFP-WPRE-pA (titer: 3×10^{12} vg/mL; Shanghai Taitool Bioscience, Shanghai, China) was injected bilaterally into the dorsolateral striatum (relative to bregma; first site: AP = +1.3 mm, ML = ±3.6 mm; second site: AP = +0.3 mm, ML = ±4.0 mm) or dorsomedial striatum (first site: AP = +1.5 mm, ML = ±2.5 mm; second site: AP = +0.5 mm, ML = ±2.7 mm). Each site consisted of two depths (DV = -4.6 mm, -4.0 mm, relative to the brain surface), and 250–300 nL of virus was injected at each depth at a rate of 50 nL/min. After each injection, the pipette was left in place for 10 min before slow retraction. Craniotomies were sealed with Kwik-Cast silicone sealant (World Precision Instruments) after all injections at a site were completed. The scalp was sutured and rats were allowed to recover in their home cages. Flunixin meglumine (2.5 mg/kg, subcutaneous or s.c.; QianShou Bio, Wuhan, China) was administered immediately post-surgery and daily for 3–5 days for analgesic effects, alongside ceftriaxone sodium (30 mg/kg, s.c.; Yuekang Duozhi, Beijing, China) to prevent infection. Body weights were monitored daily until full recovery.

Optical fiber implantation

After a minimum of 2 weeks of recovery, the scalp incision was reopened, and the skull surface was cleaned as described for virus injections. Four stainless-steel anchor screws (1.2 mm diameter; Yuyan Bio, Shanghai, China) were inserted into the skull for stability. 200-μm-diameter fiber-optic cannulae (NA 0.37; InPer Technologies, Hangzhou, China) were implanted bilaterally targeting the dorsal striatum at the following coordinates (relative to bregma): AP = +0.8 mm, ML = ±4.0 mm, DV = -3.9 mm. The craniotomies were sealed with Kwik-Cast, and the ferrules were secured to the skull using Super-Bond C&B dental adhesive (Sun Medical Co., Ltd., Shiga, Japan). A protective layer of dental cement (Jet Denture Repair; Lang Dental, Wheeling, IL, USA) was applied over the exposed skull and screws. Rats were allowed to recover under a heated lamp (35–37°C) until fully ambulatory (15–30 min).

Electrode implantation

Several variants of electrode implants were used for DLS recordings across rats. Custom-made 16-channel fixed microwire arrays (MWAs, nickel-iridium, BioSignal, Nanjing, China) were implanted in 4 rats. For combined optogenetic and electrophysiological recordings in the striatum, 16-channel fixed MWAs (Hongkong Plexon, China) integrated with a 200-μm optical fiber were implanted in 3 rats (Figure S2b). In 2 rats, 32-channel silicon probes (Diagnostic Biochips) were mounted on a movable drive (Micro Linear Drive, Janelia) and implanted. Coordinates of these electrode implants were reported previously (Figure 2 in Zheng et al.[19]). In 2 additional rats, an immobile Neuropixels probe 2.0 (IMEC, Leuven, Belgium) was implanted using a published protocol[79].

Surgical procedures followed standard stereotaxic methods (as described above). Two ground screws (with a silver wire soldered to each) were implanted bilaterally in the skull above the cerebellum, ensuring contact with brain tissue for reference and grounding. Target electrodes were implanted contralateral to the preferred paw at the following coordinates (relative to bregma): AP = +0.8 mm, ML = 4.0 mm. Fixed arrays were inserted to a final depth of -4.0 to -4.5 mm (relative to the brain surface), adjusted during implantation when large-amplitude spikes (> 100 μV) were observed on the recording system. The silicon probe was lowered to an initial depth of 2.6 mm (relative to the brain surface) and subsequently advanced in steps of 50 μm after each recording session. The Neuropixels probes, mounted on a reusable drive (3Dneuro)[79], were inserted to a depth of 5.5 mm (relative to the brain surface) with a 6° angle in both the anterior–posterior and medial–lateral planes and remained immobile thereafter. The craniotomy and the electrode were sealed with petroleum jelly (Vaseline) and bone wax. Neural recordings were performed after one week of post-implantation recovery.

For SNr recordings, movable tetrode arrays (Kedou Biotech, Hangzhou, China; stainless steel, 12.5-μm diameter wires, polyimide-coated) were used in an additional cohort of rats. These

consisted of 16-channel (4 tetrodes) or 32-channel (8 tetrodes) configurations mounted on a microdrive. Target coordinates were (relative to bregma): AP = -5.2 mm, ML = ±2.4 mm. Electrodes were initially lowered to a depth of -7.3 mm (relative to the brain surface) and advanced in steps of 50 μm simultaneously after each recording session to optimize yield.

Multi-channel recordings from the MWA, tetrode, or Si probes were conducted using a digital amplifier (Cereplex Direct, Blackrock Neurotech, Salt Lake City, UT, USA). Neuropixels recordings were conducted with a PXIe-based system (National Instruments, Austin, TX, USA) and acquired with SpikeGLX software environment (Janelia Research Campus).

Neural data analysis

Inclusion criteria

All chronic recordings were screened to exclude duplicate units recorded across multiple sessions. For Neuropixels data, 10–11 sessions per animal were included. An automated algorithm (Huang et al., *unpublished, preprint will be uploaded soon*), followed by manual curation, was used to identify and remove units repeated across sessions, ensuring only unique units were included for population analysis. Additionally, units were excluded if $> 2\%$ of their spikes' inter-spike intervals (ISIs) were < 3 ms. For all DLS units, the median ISI violation rate was 0.1% (IQR: 0–0.4%, $n = 593$ putative SPNs); for all SNr units, the median ISI violation rate was 0.1% (median, IQR: 0.1–0.5%, $n = 300$ SNr units)

Spike waveform analysis

Spike waveforms were inverted such that negative potential was oriented upward (Figure 1f). Spike width was quantified as the full width at half maximum (FWHM). To distinguish units with distinct waveform shapes, principal component analysis (PCA) was applied to the waveforms of all units within a given brain region (DLS or SNr), treating voltage values at each time point as features. Each unit's average waveform was then projected into the resulting PCA space for low-dimensional visualization. A scatter plot of the projection onto the first principal component (PC1) versus FWHM was used to separate putative spiny projection neurons (SPNs) from non-SPNs. Units were clustered into two groups with the density-based method HDBSCAN[80]. Unclustered data points were assigned to the nearest cluster based on proximity. Putative SPNs were identified as the cluster exhibiting broader spike widths (Figure 1g).

Spike rate modulation by behavioral events (GLM)

To investigate how behavioral events modulated neuronal spike rates during task performance, spike counts were quantified within pre- and post-event time windows relative to key behavioral

events using a generalized linear model (GLM) (see Figure S2a). The events and their respective time windows were (in seconds): (1) approach/lift, $[-2, -1]$ (pre) and $[-1, 0]$ (post) relative to lever press; (2) press, $[-0.5, 0]$ (pre) and $[0, 0.5]$ (post) relative to lever press; (3) trigger/release, $[-0.25, 0]$ (pre) and $[0, 0.25]$ (post) relative to trigger stimulus; (4) poke, $[-1, 0]$ (pre) and $[0, 1]$ (post) relative to port nose-poke. Events with fewer than 20 total spikes across trials were excluded to ensure reliable parameter estimation.

Spike count (spike_count$_{ij}$) was treated as a random variable from a Poisson process: Poisson(μ_{ij}). The goal was to determine whether μ is modulated by the event time point (post relative to pre) for each event. A GLM with log-link was fitted using the "fitglm" function (MATLAB, MathWorks) for each event separately. For an event, if either pre or post window had zero counts in > 50% of trials, we added 1 to both windows to stabilize fitting. The model included a fixed effect for event time point (pre: 0; post: 1) and an offset for window duration:

$$\log(\mu_{ij}) = \beta_0 + \beta_1 \text{time_point}_{ij} + \log(\text{duration}_i) \tag{1}$$

where the response variable spike_count$_{ij}$ follows Poisson(μ_{ij}) distribution; i indexes the time window (pre: i = 1, post: i = 2) for trial j; β_0 represents the fixed intercept; β_1 is the fixed-effect coefficient for the event time point; time_point$_{ij}$ is the indicator variable for pre or post time window (pre: 0, post: 1); and duration$_i$ is the duration (in seconds) of the respective time window (e.g., 0.25 s for the trigger/release pre and post windows). The coefficient β_1 represents the log-fold change in spike rate between post- and pre-event windows.

A contrast on β_1 was evaluated with a two-sided Wald test ("coefTest" function) to test the null hypothesis: $\beta_1 = 0$, yielding a p-value that indicates whether that unit's spike rate changed between post- and pre-windows for that event. To control the false discovery rate (FDR) at 0.05, the Benjamini-Hochberg procedure[81] was applied across all units and events within a brain region (DLS or SNr) to derive a critical threshold; unit-event pairs with p-values below the threshold were deemed significantly modulated (cf. Figure 1l).

SDF and warping

Spike times were convolved with a Gaussian kernel ($\sigma = 50$ ms) to obtain a smoothed spike density function (SDF). SDFs were aligned to event times to obtain a peri-event SDF, with 95% CIs derived from bootstrap resampling (1000 iterations). To average trials with different reaction times and reward retrieval durations, SDFs were linearly-warped to target times (median reaction time or reward retrieval duration across all trials at the animal level; and across animals for population averages)[82]. Let $t = t_1, t_2, \ldots, t_n$ be the time points of the $f(t) = SDF(t)$ for the current trial, and let the target time points be $t' = t'_1, t'_2, \ldots, t'_k$. The scaling factor s was applied to warp the SDF, yielding $SDF_{\text{warp}}(t')$, denoted as $f_{\text{warp}}(t')$, where $t' = t'_1, \ldots, t'_k$, as follows:

$$\mathrm{f}_{\text{warp}}(t'_i) = (\lceil i \cdot s \rceil - i \cdot s) \cdot \mathrm{f}(\lfloor i \cdot s \rfloor) + (i \cdot s - \lfloor i \cdot s \rfloor) \cdot \mathrm{f}(\lceil i \cdot s \rceil), \tag{2}$$

where $s = \frac{t_n - t_1}{t'_k - t'_1}$ and $\lceil \cdot \rceil$ and $\lfloor \cdot \rfloor$ are the ceiling and floor functions, respectively.

Units were classified as positively modulated if the maximum of their mean-subtracted average SDF (computed from 750- and 1500-ms trials) exceeded the absolute value of the minimum; otherwise, they were classified as negatively modulated. For colormaps showing ranked activity of DLS or SNr neurons (Figures 1k and 7j), the warped SDF, $SDF_{\text{warp}}(t)$, was mean-subtracted and soft-normalized by division by $(r+c)$, where r was the min-max range and c was a constant ($c=5$)[83]. To order units by response timing, data from correct trials in the 750 ms-FP condition were used to order units by the first time each unit's mean-subtracted SDF crossed a threshold (75% of the maximum for positively modulated units or 75% of the minimum for negatively modulated units). The same order was then applied to the 1500 ms-FP condition.

PCA

Neural population activity was analyzed using PCA to identify low-dimensional manifolds that capture the dominant patterns of variance across units. Unlike prior work[19], to avoid mixing different behavioral regimes, PCA spaces were constructed separately for periods dominated by forelimb movements (lever press, hold, release; from 2.5 s before lever press to lever release) versus whole-body movements (reward retrieval; from lever release to 1 s after nose-poke). For each of the two behavioral epochs, soft-normalized SDFs from included units were stacked into a matrix of size time points × units, and PCA was applied using MATLAB's "pca" function, treating each unit (column) as a covariate, yielding principal components (PCs) ordered by explained variance. Population activity was then projected onto the top 4 PCs for visualization (Figure 1l), which revealed individual PCs aligning with distinct behavioral features, such as forelimb lift initiation or reward retrieval movement.

To identify subpopulations contributing significantly to behaviorally coupled PCs (Figure 1m), units were selected based on the magnitudes of their PCA loadings (weights w_i; $i = 1, 2, 3, \ldots$ indexes the PCs) in the coefficient matrix. Thresholds were empirically pre-specified for different PCs. Loadings were taken from PCA on activity aligned to lever press for lift/hold/trigger phases, and to nose-poke for retrieval:

(1) *Lift* units (selective for pre-press paw-lifting movement):
    DLS: ($w_2 > 0.05$)
    SNr (positively modulated): ($w_2 > 0.05$)
    SNr (negatively modulated): ($w_2 < -0.05$)

(2) *Hold* units (selective for sustained press):

DLS: (w_1 > 0.05)

SNr (positively modulated): (w_1 > 0.05)

SNr (negatively modulated): (w_1 < -0.05)

(3) *Trigger/Release* units (selective for trigger stimulus and lever release):

DLS: (w_2 < 0.025 and w_3 > 0.05)

SNr (positively modulated): (w_3 < -0.05)

SNr (negatively modulated): (w_3 > 0.05)

(4) *Retrieval* units (selective for post-release reward retrieval):

DLS: ($w_1 < -0.075$ or $w_2 > 0.075$ or $w_3 > 0.075$)

SNr (positively modulated): ($w_1 < -0.075$ or $w_2 > 0.075$ or $w_3 < -0.075$)

SNr (negatively modulated): ($w_1 > 0.075$ or $w_2 < -0.075$ or $w_3 > 0.075$)

This resulted in partially overlapping subsets of units per phase, each enriched for functional relevance to the associated behavioral events. The overlaps are illustrated in Venn diagrams (Figure S2d,g). Substantial overlap indicates that a unit showed multi-event modulation.

Mapping firing rate to movement trajectories

Following alignment of video frames to behavioral timestamps, video clips were extracted around each lever press: -5 to +5 s for top-view videos, and -2 to +2 s for side-view videos. Body-part pose models were trained on selected frames and videos were tracked using DeepLabCut[42]. Tracked body parts were then manually inspected and curated via a custom MATLAB GUI to ensure high-quality trajectories (e.g., excluding occluded segments). Head position was defined as the midpoint between the two ears. For each video clip, the $x-y$ coordinates of tracked parts were stored in a table with each row representing a frame.

Discrete spike times were convolved with a Gaussian kernel ($\sigma = 50$ ms) to obtain continuous SDF (in Hz). The tracking arena was discretized into spatial bins: 1 × 1 mm for top-view trajectories and 0.33 × 0.33 mm for side-view trajectories. For each trajectory segment, head positions were linearly interpolated to SDF's timestamps. For each spatial bin, occupancy time was calculated as the total time during which the interpolated head position fell within the bin boundaries. The firing rate was estimated from the integral of the SDF over time (C_b) and the occupancy duration (T_b) in bin b, aggregated over all trials (Figure 2g; Figure S3g). A 2-D Gaussian kernel ($\sigma = 1$ pixel) was applied for smoothing:

$$\tilde{r}_b = \frac{(G_\sigma * C)_b}{(G_\sigma * T)_b + \lambda} \tag{3}$$

where $(G_\sigma * C)_b$ denotes the 2-D convolution of C with the Gaussian kernel, evaluated at bin b; $\lambda = 100$ ms is a ridge constant that stabilizes estimates in unvisited or sparsely visited bins; and $\tilde{r}_b$ is the estimated firing rate when the rat traversed bin b.

Optogenetic stimulation during lever approach

Hardware and experiment pipeline

An infrared sensor (FQD-31NO, Luo Shida Sensor, Dongguan, China) was positioned above the lever to detect rat's approach. Once detected, in a small proportion of trials (<10%), laser stimulation (473 nm) was triggered. The stimulation consisted of a 2.2-s train at 40 Hz with 5-ms pulses (DPSS laser, MBL-FN-473, Changchun New Industries Optoelectronics Technology Co., Ltd., Changchun, China). Laser light was delivered to the brain through an optical fiber (250 μm; NA: 0.37). Laser power was calibrated at the tip each day before the experiment and was set to 20-mW peak, yielding 4-mW average power during the laser pulse train. To minimize visual confounds, A masking blue LED flash (20-Hz, 5-ms pulse, 4–6 s), triggered upon approach, was presented in both NoStim and PhotoInh trials.

Forelimb movement was recorded with high-speed video at 100 fps (Camera: MER-160-227U3M, Daheng Imaging, China; Acquisition: StreamPix 7, NorPix, Montreal, Canada). Post-acquisition alignment was performed using an infrared signal locked to the trigger stimulus. Forelimb movement was tracked using DeepLabCut[42].

A polyvinylidene fluoride (PVDF) vibration sensor (LDT0-028k, TE Connectivity) was glued to the end of a lever. The electrical signal was amplified with an amplifier module (PVA103, Shenzhen Vkinging Electronics Co., Ltd, China), digitized (PCIe-6341, National Instruments), and stored with WaveSurfer (Janelia). Using simultaneously recorded video-derived lever position, a linear model converted the sensor voltage signal to lever position ($R^2 > 0.98$ on testing data; Figure S12).

Approach-to-press duration analysis (t_{a2p}; Figure 3h)

Approach-to-press duration (t_{a2p}) was computed per trial as the elapsed time between the approach detection and the lever press time recorded by Bpod. Outliers were excluded if $|t_{\text{a2p}} - \text{median}(t_{\text{a2p}})| > 5 \times \text{MAD}(t_{\text{a2p}})$. The effect of DLS photo-inhibition on the total duration from approach detection to lever press (t_{a2p}) was evaluated using a linear mixed-effects (LME) model ($t_{\text{a2p}} \sim$ StimType + (1 + StimType | anm)), which included stimulation type (StimType, 0 for NoStim and 1 for PhotoInh) as a fixed effect, with random intercepts and slopes for StimType varying by animal (anm) to account for individual variability. The model is:

$$t_{ij} = \beta_0 + \beta_1 \,\text{StimType}_{ij} + u_{0j} + u_{1j} \,\text{StimType}_{ij} + \varepsilon_{ij} \tag{4}$$

where t_{ij} denotes t_{a2p} for trial i in animal j, β_0 is the fixed intercept (baseline for NoStim), β_1 is the fixed effect of StimType, u_{0j} and u_{1j} are random intercepts and slopes for animal j, and ϵ_{ij} is the residual error. Random effects are assumed to follow a multivariate normal distribution: $(u_{0j}, u_{1j}) \sim \mathcal{N}(0, \Sigma)$, where Σ is the variance-covariance matrix, and residuals are normally distributed: $\varepsilon_{ij} \sim \mathcal{N}(0, \sigma^2)$. The same assumptions were used for the other LME models.

Velocity analysis (Figure 3i)

Forepaw velocity during the lifting phase was analyzed in a subset of rats ($n = 16$) with unobstructed forepaw tracking. Velocity was defined as the average speed (cm/s) over the trajectory path from 3.5 cm below the lift-peak position to the lift-peak position (total path length along the trajectory divided by time). An LME model (Velocity ~ StimType + (1 + StimType | anm)) was fitted with StimType as a fixed effect and random intercepts and slopes for StimType by animal:

$$v_{ij} = \beta_0 + \beta_1 \,\text{StimType}_{ij} + u_{0j} + u_{1j} \,\text{StimType}_{ij} + \varepsilon_{ij} \tag{5}$$

where v_{ij} is the observed velocity for trial i in animal j.

Segmented duration analysis (t_{a2pk} and t_{pk2p}; Figure 3j)

To dissect t_{a2p}, each trial's t_{a2p} was split into two segments: from approach to lift peak (t_{a2pk}) and from lift peak to lever press (t_{pk2p}). Segment type was treated as a factor (DurationType: a2pk or pk2p). An LME model (duration $\sim$ StimType × DurationType + (1 + StimType | anm) + (1 | anm:trial)) was fitted to assess the interaction between StimType and DurationType, with a random intercept and StimType slope by animal, plus a trial-level random intercept (anm:trial) to account for two repeated measures within a trial:

$$\begin{aligned} t_{ijk} = {} & \beta_0 + \beta_1 \,\text{StimType}_{jk} + \beta_2 \,\text{DurationType}_i + \beta_3 \left(\text{StimType}_{jk} \times \text{DurationType}_i\right) \\ & + u_{0j} + u_{1j} \,\text{StimType}_{jk} + v_{jk} + \varepsilon_{ijk} \end{aligned} \tag{6}$$

where t_{ijk} is the duration for DurationType i in animal j and trial k; u_{0j}, u_{1j} are the animal-level random intercept and random slope for StimType; and v_{jk} is the random intercept per trial k within animal j.

Effect of different stimulation sides on t_{a2p} (Figure S5e)

To examine the effects of photo-inhibition applied to different stimulation sides (bilateral, contralateral, or ipsilateral; bilateral as reference) on t_{a2p}, an LME model was fitted with StimType

and StimSide as fixed effects, along with their interaction: $t_{\text{a2p}} \sim$ StimType × StimSide + (1 + StimType | anm). Random intercepts and slopes for StimType varied by animal (anm). The model equation is:

$$\begin{aligned} t_{ij} = \beta_0 + \beta_1 \,\text{StimType}_{ij} + \beta_2 \,\text{StimSide}_{\text{contra},ij} + \beta_3 \,\text{StimSide}_{\text{ipsi},ij} \\ + \beta_4 \left(\text{StimType}_{ij} \times \text{StimSide}_{\text{contra},ij}\right) + \beta_5 \left(\text{StimType}_{ij} \times \text{StimSide}_{\text{ipsi},ij}\right) \\ + u_{0j} + u_{1j} \,\text{StimType}_{ij} + \varepsilon_{ij} \end{aligned} \tag{7}$$

where t_{ij} is t_{a2p} for trial i in animal j.

Optogenetic stimulation during forepaw lifting

A second side camera (MER-160-227U3M, Daheng Imaging, China) positioned next to the main side camera captured the paw lifting process within a 20 × 15 cm field of view at 50 fps. Frames were streamed to Bonsai[49], where a smaller 7 × 4 cm region was analyzed. Bonsai integrated DeepLabCut-Live[48] to estimate the coordinates and detection likelihood of the selected forepaw (left or right). When the paw position exceeded a predefined threshold and the detection likelihood was $>75\%$ for three consecutive frames, Bonsai transmitted a trigger signal to the Bpod state machine as a SoftCode event. Bpod then determined whether to initiate laser stimulation based on a predefined probability ($<10\%$). The threshold was adjustable to allow stimulation at different phases of the reaching movement (Figure 4j–o).

Drop ratio analysis (Figure 4g)

A drop event was counted when the vertical paw position fell below a predefined threshold (50–70% of the height from baseline to the global peak position) after the lift's local peak. The drop ratio (p_{drop}) was computed for each condition (StimType per animal). Paired differences between NoStim and PhotoInh conditions were assessed using a two-sided Wilcoxon signed-rank test on the p_{drop}.

Lift-to-press duration analysis (t_{l2p}; Figure 4i)

The effect of DLS photo-inhibition on the duration from lift detection to lever press (t_{l2p}) was evaluated using a LME model: $t_{\text{l2p}} \sim$ StimType + (1 + StimType | anm). The model included stimulation type (StimType, 0 for NoStim and 1 for PhotoInh) as a fixed effect, with random intercepts and slopes for StimType varying by anm:

$$t_{ij} = \beta_0 + (\beta_1 + u_{1j}) \,\text{StimType}_{ij} + u_{0j} + \varepsilon_{ij} \tag{8}$$

where t_{ij} is the t_{l2p} for trial i in animal j.

Segmented duration analysis (t_{l2pk} and t_{pk2p}; Figure 4i)

To dissect t_{l2p}, each trial's t_{l2p} was split into two segments: from lift to lift-peak (t_{l2pk}) and from lift-peak to lever press (t_{pk2p}). Segment type was treated as a factor (DurationType factor: l2pk or pk2p). An LME model (duration ~$ StimType × DurationType + (1 + StimType | anm) + (1 | anm:trial)) was fitted to assess the interaction between StimType and tType:

$$\begin{aligned} t_{ijk} = \beta_0 + \beta_1 \,\text{StimType}_{jk} + \beta_2 \,\text{DurationType}_i + \beta_3 \left(\text{StimType}_{jk} \times \text{DurationType}_i\right) \\ + u_{0j} + u_{1j} \,\text{StimType}_{jk} + v_{jk} + \varepsilon_{ijk} \end{aligned} \tag{9}$$

where t_{ijk} is the duration for DurationType i in animal j and trial k.

Peak-to-press duration at different stages (Figure 4o)

The effect of photo-inhibition on t_{pk2p} was examined at different inhibition stages along the reach trajectory. Inhibition stage was treated as a factor Stage (0 for inhibition early in a reaching movement or 1 for inhibition late in a reaching movement). An LME model (duration ~ StimType × Stage + (1 + Stim_type | anm)) was fitted to assess the interaction between StimType and Stage:

$$\begin{aligned} t_{ij} = \beta_0 + \beta_1 \,\text{StimType}_{ij} + \beta_2 \,\text{Stage}_{ij} + \beta_3 \left(\text{StimType}_{ij} \times \text{Stage}_{ij}\right) \\ + u_{0j} + u_{1j} \,\text{StimType}_{ij} + \varepsilon_{ij} \end{aligned} \tag{10}$$

where t_{ij} is the t_{pk2p} for trial i in animal j.

Effect of different stimulation sides on t_{l2p} (Figure S5j)

To examine the effects of photoinhibition applied to different stimulation sides (bilateral, contralateral, ipsilateral) on t_{l2p}, an LME model was fitted: $t_{\text{l2p}} \sim$ StimType × StimSide + (1 + StimType | anm). The model equation is:

$$\begin{aligned} t_{ij} = \beta_0 + \beta_1 \,\text{StimType}_{ij} + \beta_2 \,\text{StimSide}_{\text{contra},ij} + \beta_3 \,\text{StimSide}_{\text{ipsi},ij} \\ + \beta_4 \left(\text{StimType}_{ij} \times \text{StimSide}_{\text{contra},ij}\right) + \beta_5 \left(\text{StimType}_{ij} \times \text{StimSide}_{\text{ipsi},ij}\right) \\ + u_{0j} + u_{1j} \,\text{StimType}_{ij} + \varepsilon_{ij} \end{aligned} \tag{11}$$

where t_{ij} is t_{l2p} for trial i in animal j.

Optogenetic stimulation coupled to trigger stimulus

For trigger-coupled photo-inhibition (Figure 5), the trigger stimulus activated the Bpod's scheduled waves. Laser stimulation was applied in $<25\%$ of trials per session, randomly assigned to different events such as approach, lever-press, or trigger in the same session.

Reaction-time (RT) outliers exceeding 25 $\times$ MAD from the median (>4.427 s) were excluded. RTs $<$ 0.1 s were also excluded. Photo-inhibition trials (and corresponding NoStim trials) were

classified as 'Early' (≤ 60 stimulation trials) or 'Late' (> 60) to define the fixed factor StimGroup. FP is a categorical factor with two levels: Short$=750$ ms and Long$=1500$ ms. Log-transformed RT (logRT) data were fitted with an LME model (logRT $\sim$ StimType × StimGroup × FP + (1 + StimType | anm)):

$$\begin{aligned} y_{ij} = & \beta_0 + \beta_1 \,\text{StimType}_{ij} + \beta_2 \,\text{StimGroup}_{ij} + \beta_3 \,\text{FP}_{ij} \\ & + \beta_4 \left(\text{StimType}_{ij} \times \text{StimGroup}_{ij}\right) + \beta_5 \left(\text{StimType}_{ij} \times \text{FP}_{ij}\right) + \beta_6 \left(\text{StimGroup}_{ij} \times \text{FP}_{ij}\right) \\ & + \beta_7 \left(\text{StimType}_{ij} \times \text{StimGroup}_{ij} \times \text{FP}_{ij}\right) + u_{0j} + u_{1j} \,\text{StimType}_{ij} + \varepsilon_{ij} \end{aligned} \tag{12}$$

where y_{ij} is logRT for trial i in animal j.

Reward retrieval duration and locomotor behavior

A top-view camera operating at 100 fps captured videos using Streampix 7 to monitor locomotion. DeepLabCut was used to track body parts, determining the rat's head location and direction. Movement paths were derived from the positions of the ears, with head direction defined as the vector orthogonal to the ear-to-ear line and pointing toward the nose. Instantaneous velocity of the head for each frame was calculated as the Euclidean displacement between the current head location and the head location one frame ahead, divided by the time interval (10 ms). The velocity time series was smoothed using a moving average filter (centered window of 25 samples or 250 ms). In release-coupled photo-inhibition, mean velocity for each trial was computed as the average instantaneous velocity from lever release to 1 s after lever release, capturing the period of active movement. For photo-inhibition near the reward port triggered by an IR detector (near-poke-coupled), mean velocity was computed as the average from detection to 0.5 s after detection. Movement path length was calculated as the cumulative Euclidean distance from lever release (or IR detection) to water-port nose-poke. Photo-inhibition was applied bilaterally or unilaterally (ipsilateral or contralateral to the turning direction) in an interleaved, randomized order across sessions.

These release- or near-poke-coupled photo-inhibition experiments had a smaller sample size (n=6) than the forelimb reaching experiments ($n=25$ tested, $n=16$ tracked) because our initial focus was on the forelimb movement; whole-body locomotion tests were added later after observing increased reward retrieval duration under trigger-coupled photo-inhibition.

Three LME models with the same formula were applied to analyze movement path length, velocity, and retrieval duration. Measurements were obtained from multiple trials across multiple sessions for each rat. Each LME model (Metric $\sim$ StimType × StimSide + (1 + StimType | anm)) included StimType and StimSide (bilateral, ipsilateral, contralateral to the turning direction; with bilateral as the reference level) as fixed effects, and animal as a random effect. The slope for StimType was allowed to vary by rats. The model for each measurement y is given by:

$$
\begin{aligned}
y_{ij} = & \beta_0 + \beta_1 \,\text{StimType}_{ij} + \beta_2 \,\text{StimSide}_{\text{ipsi},ij} + \beta_3 \,\text{StimSide}_{\text{contra},ij} \\
& + \beta_4 \left(\text{StimType}_{ij} \times \text{StimSide}_{\text{ipsi},ij}\right) + \beta_5 \left(\text{StimType}_{ij} \times \text{StimSide}_{\text{contra},ij}\right) \\
& + u_{0j} + u_{1j} \,\text{StimType}_{ij} + \varepsilon_{ij}
\end{aligned} \tag{13}
$$

where y_{ij} is the metric (path length, mean velocity, or retrieval duration) for trial i in animal j; all other terms are defined as in the previous models. The same model specification applies to both release- and near-poke-coupled photo-inhibition (Figure 6g–i, n–p).

A similar model was fitted for reward retrieval duration under trigger-coupled photo-inhibition (Figure S8c). A simplified model excluding StimSide (bilateral only) was used for kinematics analysis during trigger-coupled photo-inhibition (Figure S8h–j).

Statistics

LME or linear models were analyzed using R ("lme4" and "lmerTest" packages). Significance of the fixed effect (e.g., β_1 in Equation 4) was assessed via a *t*-test with Satterthwaite approximation for degrees of freedom and the estimated marginal means for PhotoInh - NoStim contrast (effect size) were computed using "emmeans" package, with SEM derived from the model. P-values were adjusted with Holm's method when multiple tests were performed (e.g., relative effect size among different StimSide, Figure S7f–h). Effect size was reported for all statistical tests. GLM-based analysis of spike count modulation was conducted using MATLAB, as detailed above.

Acknowledgements

We thank Dr. Mark Laubach for sharing code for behavioral training and for many fruitful discussions. We thank Qiang Zheng for help implementing real-time pose tracking. This work was supported by the National Natural Science Foundation of China (32070983, 32271052, 32571183), the Natural Science Foundation of Beijing Municipality (5212007), the Peking-Tsinghua Center for Life Sciences, and the State Key Laboratory of Membrane Biology.

Supplemental Materials

1. Figure S1 | SRT behavior of rats.
2. Figure S2 | Behavioral event-modulation of neural activity in DLS and SNr.
3. Figure S3 | Striatal neural activity tracks rat's movement in a different rat.
4. Figure S4 | Optogenetic inhibition of DLS via activating inhibitory interneurons.
5. Figure S5 | Unilateral versus bilateral DLS photo-inhibition during approach or lift.
6. Figure S6 | Unilateral versus bilateral DLS photo-inhibition coupled to trigger stimulus.
7. Figure S7 | Unilateral versus bilateral DLS photo-inhibition during reward retrieval.
8. Figure S8 | Trigger-coupled DLS photo-inhibition slows down reward retrieval and locomotion.
9. Figure S9 | Control experiments.
10. Figure S10 | Bilateral DMS photo-inhibition during approach or reward retrieval.
11. Figure S11 | Press-coupled DLS photo-inhibition increases anticipatory responses.
12. Figure S12 | Piezo-sensor signal mapping to lever position.
13. Video S1 | Comparison of forelimb reaching in a no-stimulation trial (left) and an approach-coupled DLS photo-inhibition trial (right).
14. Video S2 | Comparison of forelimb reaching in a no-stimulation trial (left) and a lift-coupled DLS photo-inhibition trial (right).
15. Video S3 | Comparison of lever release in a no-stimulation trial (left) and a trigger-coupled DLS photo-inhibition trial (right).
16. Video S4 | Comparison of reward retrieval in a no-stimulation trial (left) and a release-coupled DLS photo-inhibition trial (right).
17. Video S5 | Comparison of reward retrieval in a no-stimulation trial (left) and a trigger-coupled DLS photo-inhibition trial (right).
18. Video S6 | Comparison of reward retrieval in a no-stimulation trial (left) and a poke-coupled DLS photo-inhibition trial (right).

References

1. Tinbergen, N. *The Study of Instinct*. (Clarendon Press ; Oxford University Press, Oxford [England] : New York, 1989).
2. Hintiryan, H. *et al.* The mouse cortico-striatal projectome. *Nat Neurosci* **19**, 1100–1114 (2016).
3. Hunnicutt, B. J. *et al.* A comprehensive excitatory input map of the striatum reveals novel functional organization. *eLife* **5**, e19103 (2016).
4. BRAIN Initiative Cell Census Network (BICCN) *et al.* A multimodal cell census and atlas of the mammalian primary motor cortex. *Nature* **598**, 86–102 (2021).
5. Muñoz-Castañeda, R. *et al.* Cellular anatomy of the mouse primary motor cortex. *Nature* **598**, 159–166 (2021).
6. Lawrence, D. G. & Kuypers, H. G. J. M. THE FUNCTIONAL ORGANIZATION OF THE MOTOR SYSTEM IN THE MONKEY: I. THE EFFECTS OF BILATERAL PYRAMIDAL LESIONS. *Brain* **91**, 1–14 (1968).
7. Lawrence, D. G. & Kuypers, H. G. J. M. THE FUNCTIONAL ORGANIZATION OF THE MOTOR SYSTEM IN THE MONKEY: II. THE EFFECTS OF LESIONS OF THE DESCENDING BRAIN-STEM PATHWAYS. *Brain* **91**, 15–36 (1968).
8. Graybiel, A. M. Building action repertoires: Memory and learning functions of the basal ganglia. *Current Opinion in Neurobiology* **5**, 733–741 (1995).
9. Yin, H. H. & Knowlton, B. J. The role of the basal ganglia in habit formation. *Nat Rev Neurosci* **7**, 464–476 (2006).
10. Jog, M. S., Kubota, Y., Connolly, C. I., Hillegaart, V. & Graybiel, A. M. Building Neural Representations of Habits. *Science* **286**, 1745–1749 (1999).
11. Barnes, T. D., Kubota, Y., Hu, D., Jin, D. Z. & Graybiel, A. M. Activity of striatal neurons reflects dynamic encoding and recoding of procedural memories. *Nature* **437**, 1158–1161 (2005).
12. Schmitzer-Torbert, N. & Redish, A. D. Neuronal Activity in the Rodent Dorsal Striatum in Sequential Navigation: Separation of Spatial and Reward Responses on the Multiple T Task. *Journal of Neurophysiology* **91**, 2259–2272 (2004).
13. Mink, J. W. The basal ganglia: Focused selection and inhibition of competing motor programs. *Prog Neurobiol* **50**, 381–425 (1996).
14. Seo, M., Lee, E. & Averbeck, B. B. Action selection and action value in frontal-striatal circuits. *Neuron* **74**, 947–960 (2012).
15. Hikosaka, O., Takikawa, Y. & Kawagoe, R. Role of the Basal Ganglia in the Control of Purposive Saccadic Eye Movements. *Physiological Reviews* **80**, 953–978 (2000).
16. Dhawale, A. K., Wolff, S. B. E., Ko, R. & Ölveczky, B. P. The basal ganglia control the detailed kinematics of learned motor skills. *Nat Neurosci* **24**, 1256–1269 (2021).

17. Dudman, J. T. & Krakauer, J. W. The basal ganglia: From motor commands to the control of vigor. *Current Opinion in Neurobiology* **37**, 158–166 (2016).

18. Jurado-Parras, M.-T. *et al.* The Dorsal Striatum Energizes Motor Routines. *Current Biology* **30**, 4362–4372.e6 (2020).

19. Zheng, Q. *et al.* The Role of Striatum in Controlling Waiting during Reactive and Self-Timed Behaviors. *J. Neurosci.* **45**, (2025).

20. Rueda-Orozco, P. E. & Robbe, D. The striatum multiplexes contextual and kinematic information to constrain motor habits execution. *Nat Neurosci* **18**, 453–460 (2015).

21. Amaya, K. A. & Smith, K. S. Alternative Approaches to Understanding Habit Learning in the Dorsolateral Striatum. in *Habits* (ed. Vandaele, Y.) 141–167 (Springer International Publishing, Cham, 2024). doi:10.1007/978-3-031-55889-4_7.

22. Horn, A. K. E. & Straka, H. Functional Organization of Extraocular Motoneurons and Eye Muscles. *Annu. Rev. Vis. Sci.* **7**, 793–825 (2021).

23. Hyland, B. I. & Jordan, V. M. B. Muscle activity during forelimb reaching movements in rats. *Behavioural Brain Research* **85**, 175–186 (1997).

24. Gilmer, J. I. *et al.* A novel biomechanical model of the mouse forelimb predicts muscle activity in optimal control simulations of reaching movements. http://biorxiv.org/lookup/doi/10.1101/2024.09.05.611289 (2024) doi:10.1101/2024.09.05.611289.

25. Miri, A. *et al.* Behaviorally Selective Engagement of Short-Latency Effector Pathways by Motor Cortex. *Neuron* **95**, 683–696.e11 (2017).

26. Cohen, A. H. & Gans, C. Muscle activity in rat locomotion: Movement analysis and electromyography of the flexors and extensors of the elbow. *Journal of Morphology* **146**, 177–196 (1975).

27. Gorassini, M., Eken, T., Bennett, D. J., Kiehn, O. & Hultborn, H. Activity of Hindlimb Motor Units During Locomotion in the Conscious Rat. *Journal of Neurophysiology* **83**, 2002–2011 (2000).

28. Gramsbergen, A. Posture and Locomotion in the Rat: Independent or Interdependent Development? *Neuroscience & Biobehavioral Reviews* **22**, 547–553 (1998).

29. Panigrahi, B. *et al.* Dopamine Is Required for the Neural Representation and Control of Movement Vigor. *Cell* **162**, 1418–1430 (2015).

30. Desmurget, M. & Turner, R. S. Testing Basal Ganglia Motor Functions Through Reversible Inactivations in the Posterior Internal Globus Pallidus. *Journal of Neurophysiology* **99**, 1057–1076 (2008).

31. Jin, X. & Costa, R. M. Start/Stop Signals Emerge in Nigrostriatal Circuits during Sequence Learning. *Nature* **466**, 457–462 (2010).

32. Vandaele, Y. *et al.* Distinct recruitment of dorsomedial and dorsolateral striatum erodes with extended training. *eLife* **8**, e49536 (2019).

950 33. Tecuapetla, F., Matias, S., Dugue, G. P., Mainen, Z. F. & Costa, R. M. Balanced activity in basal ganglia projection pathways is critical for contraversive movements. *Nat Commun* **5**, 4315 (2014).

951 34. Wiener, S. Spatial and behavioral correlates of striatal neurons in rats performing a self-initiated navigation task. *J. Neurosci.* **13**, 3802–3817 (1993).

952 35. Narayanan, N. S., Horst, N. K. & Laubach, M. Reversible inactivations of rat medial prefrontal cortex impair the ability to wait for a stimulus. *Neuroscience* **139**, 865–876 (2006).

953 36. Amalric, M. & Koob, G. Depletion of dopamine in the caudate nucleus but not in nucleus accumbens impairs reaction-time performance in rats. *J. Neurosci.* **7**, 2129–2134 (1987).

954 37. Tecuapetla, F., Jin, X., Lima, S. Q. & Costa, R. M. Complementary Contributions of Striatal Projection Pathways to Action Initiation and Execution. *Cell* **166**, 703–715 (2016).

955 38. Cruz, B. F. *et al.* Action suppression reveals opponent parallel control via striatal circuits. *Nature* **607**, 521–526 (2022).

956 39. Laubach, M., Wessberg, J. & Nicolelis, M. A. Cortical ensemble activity increasingly predicts behaviour outcomes during learning of a motor task. *Nature* **405**, 567–571 (2000).

957 40. Risterucci, C., Terramorsi, D., Nieoullon, A. & Amalric, M. Excitotoxic lesions of the prelimbic-infralimbic areas of the rodent prefrontal cortex disrupt motor preparatory processes. *Eur J Neurosci* **17**, 1498–1508 (2003).

958 41. Narayanan, N. S. & Laubach, M. Top-Down Control of Motor Cortex Ensembles by Dorsomedial Prefrontal Cortex. *Neuron* **52**, 921–931 (2006).

959 42. Mathis, A. *et al.* DeepLabCut: Markerless pose estimation of user-defined body parts with deep learning. *Nat Neurosci* **21**, 1281–1289 (2018).

960 43. Mizes, K. G. C., Lindsey, J., Escola, G. S. & Ölveczky, B. P. Dissociating the contributions of sensorimotor striatum to automatic and visually guided motor sequences. *Nat Neurosci* 1–14 (2023) doi:10.1038/s41593-023-01431-3.

961 44. Burke, D. A., Rotstein, H. G. & Alvarez, V. A. Striatal Local Circuitry: A New Framework for Lateral Inhibition. *Neuron* **96**, 267–284 (2017).

962 45. Tepper, J. M., Tecuapetla, F., Koós, T. & Ibáñez-Sandoval, O. Heterogeneity and Diversity of Striatal GABAergic Interneurons. *Front. Neuroanat.* **4**, (2010).

963 46. De, A., El-Shamayleh, Y. & Horwitz, G. D. Fast and reversible neural inactivation in macaque cortex by optogenetic stimulation of GABAergic neurons. *eLife* **9**, e52658 (2020).

964 47. Dimidschstein, J. *et al.* A viral strategy for targeting and manipulating interneurons across vertebrate species. *Nat Neurosci* **19**, 1743–1749 (2016).

965 48. Kane, G. A., Lopes, G., Saunders, J. L., Mathis, A. & Mathis, M. W. Real-time, low-latency closed-loop feedback using markerless posture tracking. *eLife* **9**, e61909 (2020).

966 49. Lopes, G. *et al.* Bonsai: An event-based framework for processing and controlling data streams. *Front. Neuroinform.* **9**, (2015).

967 50. O'Connor, D. H. *et al.* Neural coding during active somatosensation revealed using illusory touch. *Nat Neurosci* **16**, 958–965 (2013).

968 51. Huber, D. *et al.* Sparse optical microstimulation in barrel cortex drives learned behaviour in freely moving mice. *Nature* **451**, 61–64 (2008).

969 52. Owen, S. F., Liu, M. H. & Kreitzer, A. C. Thermal constraints on in vivo optogenetic manipulations. *Nat Neurosci* **22**, 1061–1065 (2019).

970 53. Chen, Z. *et al.* Direct and indirect pathway neurons in ventrolateral striatum differentially regulate licking movement and nigral responses. *Cell Reports* **37**, 109847 (2021).

971 54. Freeze, B. S., Kravitz, A. V., Hammack, N., Berke, J. D. & Kreitzer, A. C. Control of Basal Ganglia Output by Direct and Indirect Pathway Projection Neurons. *J. Neurosci.* **33**, 18531–18539 (2013).

972 55. Falasconi, A., Kanodia, H. & Arber, S. Dynamic basal ganglia output signals license and suppress forelimb movements. *Nature* https://doi.org/10.1038/s41586-025-09066-z (2025) doi:10.1038/s41586-025-09066-z.

973 56. Liu, D. *et al.* A common hub for sleep and motor control in the substantia nigra. *Science* **367**, 440–445 (2020).

974 57. McElvain, L. E. *et al.* Specific populations of basal ganglia output neurons target distinct brain stem areas while collateralizing throughout the diencephalon. *Neuron* **109**, 1721–1738.e4 (2021).

975 58. Hikosaka, O. GABAergic output of the basal ganglia. in *Progress in Brain Research* vol. 160 209–226 (Elsevier, 2007).

976 59. Von Krosigk, M. & Smith, A. D. Descending Projections from the Substantia Nigra and Retrorubral Field to the Medullary and Pontomedullary Reticular Formation. *Eur J Neurosci* **3**, 260–273 (1991).

977 60. Rossi, M. A. *et al.* A GABAergic nigrotectal pathway for coordination of drinking behavior. *Nat Neurosci* **19**, 742–748 (2016).

978 61. Rizzi, G. & Tan, K. R. Synergistic Nigral Output Pathways Shape Movement. *Cell Reports* **27**, 2184–2198.e4 (2019).

979 62. Lintz, M. J. & Felsen, G. Basal ganglia output reflects internally-specified movements. *eLife* **5**, e13833 (2016).

980 63. Fan, D., Rossi, M. A. & Yin, H. H. Mechanisms of Action Selection and Timing in Substantia Nigra Neurons. *J. Neurosci.* **32**, 5534–5548 (2012).

981 64. Turner, R. S. & Desmurget, M. Basal ganglia contributions to motor control: A vigorous tutor. *Current Opinion in Neurobiology* **20**, 704–716 (2010).

982 65. Robledo, P. & Féger, J. Excitatory influence of rat subthalamic nucleus to substantia nigra pars reticulata and the pallidal complex: Electrophysiological data. *Brain Research* **518**, 47–54 (1990).

983 66. Ji, Y.-W. *et al.* Differential remodeling of subthalamic projections to basal ganglia output nuclei and locomotor deficits in 6-OHDA-induced hemiparkinsonian mice. *Cell Reports* **42**, 112178 (2023).

984 67. DeLong, M. R. & Wichmann, T. Circuits and Circuit Disorders of the Basal Ganglia. *Arch Neurol* **64**, 20 (2007).

985 68. Balleine, B. W., Delgado, M. R. & Hikosaka, O. The Role of the Dorsal Striatum in Reward and Decision-Making. *J. Neurosci.* **27**, 8161–8165 (2007).

986 69. Crego, A. C. G., Amaya, K. A., Palmer, J. A. & Smith, K. S. A role for the dorsolateral striatum in prospective action control. *iScience* **27**, 110044 (2024).

987 70. Crego, A. C. G. *et al.* Complementary Control over Habits and Behavioral Vigor by Phasic Activity in the Dorsolateral Striatum. *J Neurosci* **40**, 2139–2153 (2020).

988 71. Desmurget, M. & Turner, R. S. Motor Sequences and the Basal Ganglia: Kinematics, Not Habits. *Journal of Neuroscience* **30**, 7685–7690 (2010).

989 72. Otchy, T. M. *et al.* Acute off-target effects of neural circuit manipulations. *Nature* **528**, 358–363 (2015).

990 73. Wolff, S. B. & Ölveczky, B. P. The promise and perils of causal circuit manipulations. *Current Opinion in Neurobiology* **49**, 84–94 (2018).

991 74. Guo, Z. V. *et al.* Flow of cortical activity underlying a tactile decision in mice. *Neuron* **81**, 179–194 (2014).

992 75. Pettibone, J. R. *et al.* Knock-In Rat Lines with Cre Recombinase at the Dopamine D1 and Adenosine 2a Receptor Loci. *eNeuro* **6**, ENEURO.0163–19.2019 (2019).

993 76. Hunker, A. C. *et al.* Enhancer AAV toolbox for accessing and perturbing striatal cell types and circuits. *Neuron* **113**, 1507–1524.e17 (2025).

994 77. Isett, B. R. *et al.* The indirect pathway of the basal ganglia promotes transient punishment but not motor suppression. *Neuron* **111**, 2218–2231.e4 (2023).

995 78. Thorn, C. A., Atallah, H., Howe, M. & Graybiel, A. M. Differential Dynamics of Activity Changes in Dorsolateral and Dorsomedial Striatal Loops during Learning. *Neuron* **66**, 781–795 (2010).

996 79. Vöröslakos, M., Petersen, P. C., Vöröslakos, B. & Buzsáki, G. Metal microdrive and head cap system for silicon probe recovery in freely moving rodent. *eLife* **10**, e65859 (2021).

997 80. McInnes, L., Healy, J. & Astels, S. Hdbscan: Hierarchical density based clustering. *JOSS* **2**, 205 (2017).

998 81. Benjamini, Y. & Hochberg, Y. Controlling the False Discovery Rate: A Practical and Powerful Approach to Multiple Testing. *Journal of the Royal Statistical Society: Series B (Methodological)* **57**, 289–300 (1995).

999 82. Williams, A. H. *et al.* Discovering Precise Temporal Patterns in Large-Scale Neural Recordings through Robust and Interpretable Time Warping. *Neuron* **105**, 246–259.e8 (2020).

1000 83. Churchland, M. M. *et al.* Neural population dynamics during reaching. *Nature* **487**, 51–56 (2012).

Supplemental Materials

Differential controls of forelimb versus whole-body movements by striatum

Jiaming Cao, Yujie Zhao, Jianing Yu

1. Figure S1 | SRT behavior of rats.
2. Figure S2 | Behavioral event-modulation of neural activity in DLS and SNr.
3. Figure S3 | Striatal neural activity tracks rat's movement in a different rat.
4. Figure S4 | Optogenetic inhibition of DLS via activating inhibitory interneurons.
5. Figure S5 | Unilateral versus bilateral DLS photo-inhibition during approach or lift.
6. Figure S6 | Unilateral versus bilateral DLS photo-inhibition coupled to trigger stimulus.
7. Figure S7 | Unilateral versus bilateral DLS photo-inhibition during reward retrieval.
8. Figure S8 | Trigger-coupled DLS photo-inhibition slows down reward retrieval and locomotion.
9. Figure S9 | Control experiments.
10. Figure S10 | Bilateral DMS photo-inhibition during approach or reward retrieval.
11. Figure S11 | Press-coupled DLS photo-inhibition increases anticipatory responses.
12. Figure S12 | Piezo-sensor signal mapping to lever position.
13. Video S1 | Comparison of forelimb reaching in a no-stimulation trial (left) and an approach-coupled DLS photo-inhibition trial (right).
14. Video S2 | Comparison of forelimb reaching in a no-stimulation trial (left) and a lift-coupled DLS photo-inhibition trial (right).
15. Video S3 | Comparison of lever release in a no-stimulation trial (left) and a trigger-coupled DLS photo-inhibition trial (right).
16. Video S4 | Comparison of reward retrieval in a no-stimulation trial (left) and a release-coupled DLS photo-inhibition trial (right).
17. Video S5 | Comparison of reward retrieval in a no-stimulation trial (left) and a trigger-coupled DLS photo-inhibition trial (right).
18. Video S6 | Comparison of reward retrieval in a no-stimulation trial (left) and a poke-coupled DLS photo-inhibition trial (right).

Supplemental Figure 1

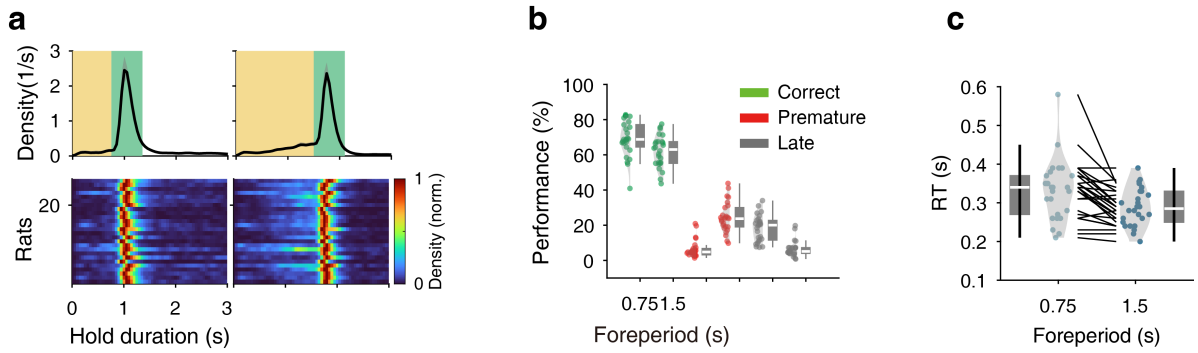

Figure S1. SRT behavior of rats. **a**, Probability density functions (PDFs) of 26 rats. Top, mean and SEM of PDFs for two FPs (left, 0.75 s; right, 1.5 s). Bottom, each row is the PDF of a single rat. Color denotes probability density (peak-normalized). **b**, Correct, premature, and late ratios. **c**, Reaction times of all rats for two FPs.

Supplemental Figure 2

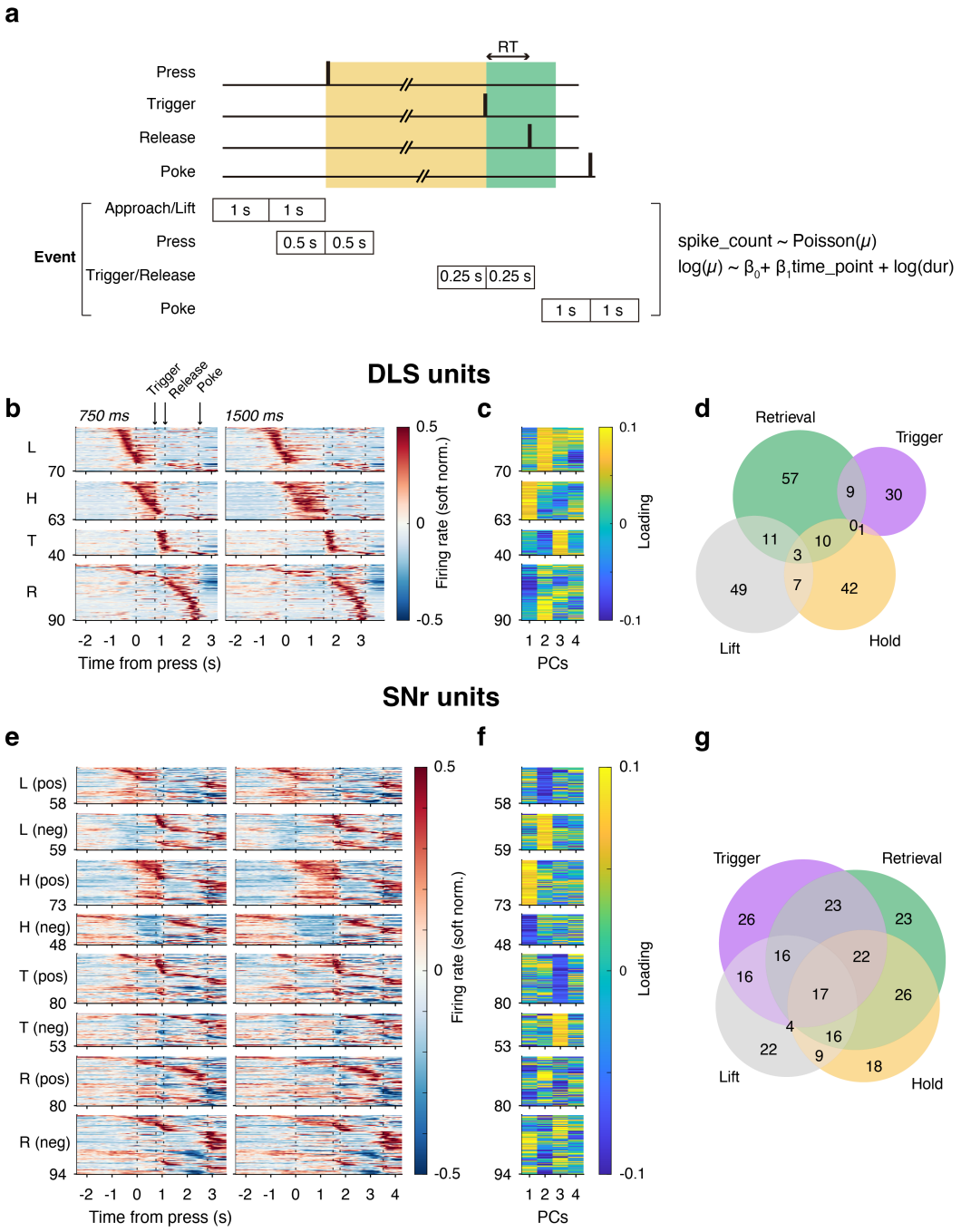

Figure S2. Behavioral event-modulation of neural activity in DLS and SNr. **a**, Diagram illustrating the construction of event time windows for analyzing spike rate modulation by a GLM. **b**, Left, Colormap showing the normalized SDFs of units selected by PCA loadings in Figure 1n. L: Lift; H: Hold; T: Trigger/Release; R: Retrieval. **c**, Projection loadings of these selected units. **d**, Venn diagram illustrating the overlap of selected units. **e–g**, Same as **b–d** for SNr units. Positively and negatively modulated units are shown separately for each functional category.

Supplemental Figure 3

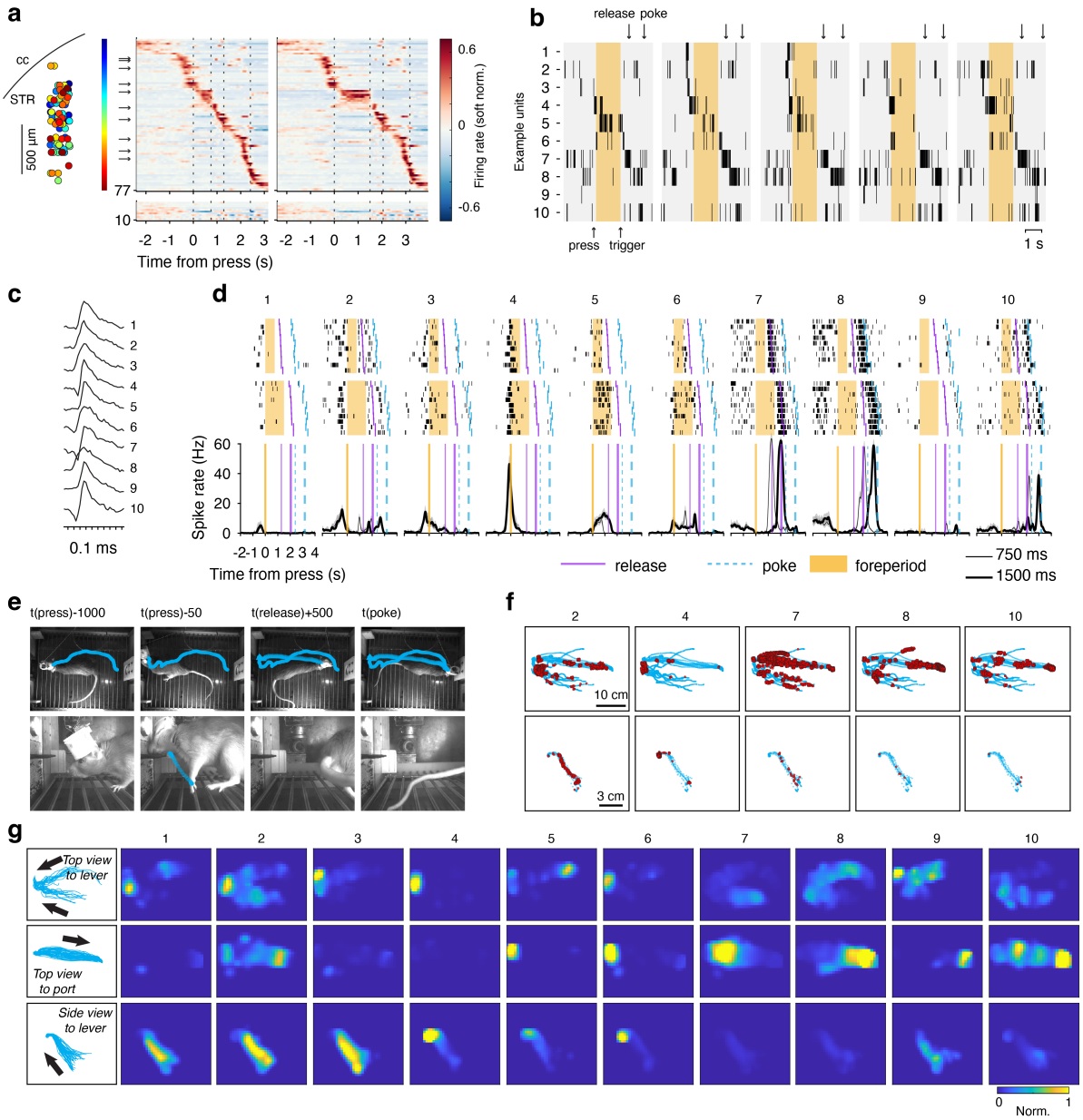

Figure S3. Striatal neural activity tracks rat's movement in a different rat. As in Figure 2 from chronic Neuropixels probe recordings in a different rat. All data are simultaneously recorded units from a single session.

Supplemental Figure 4

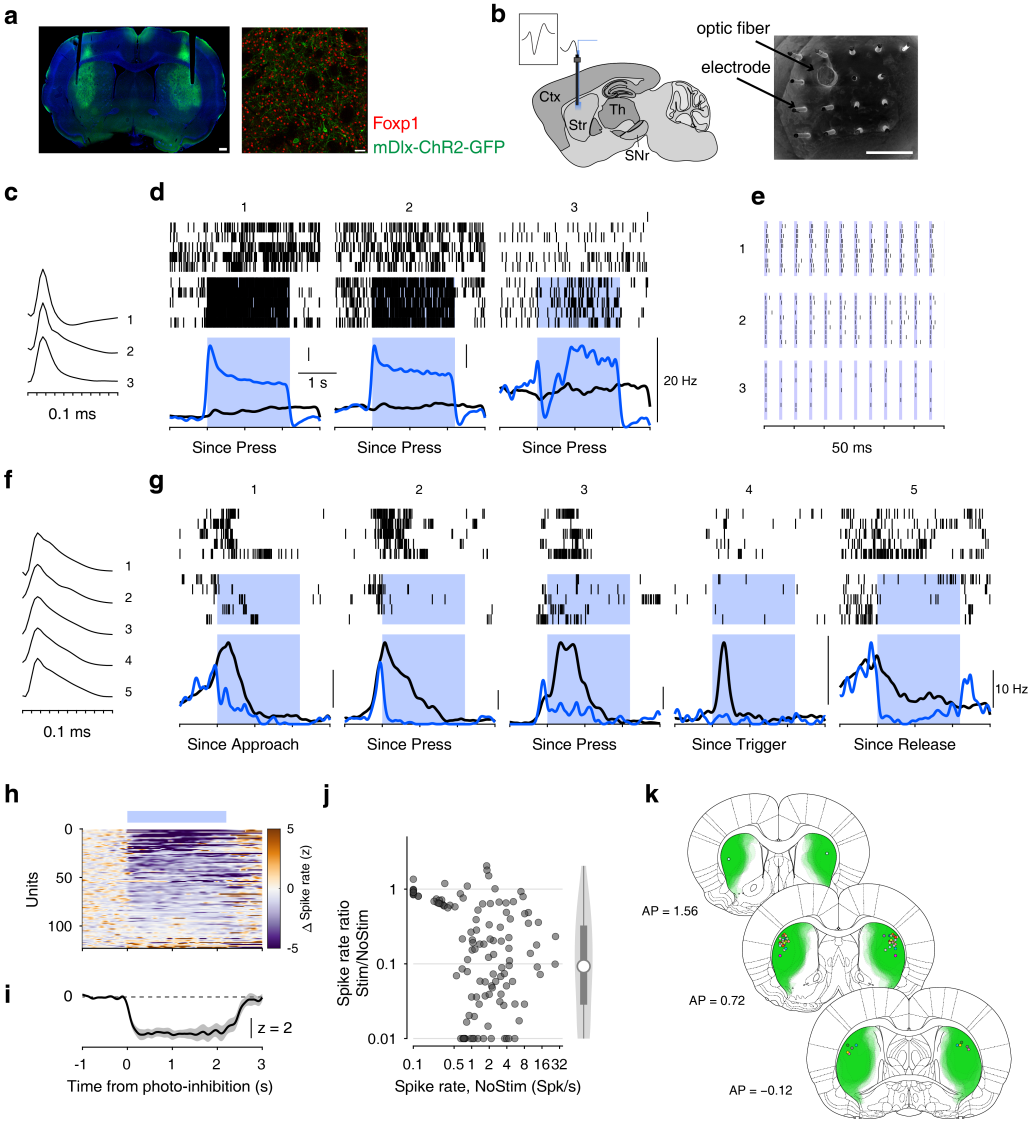

Figure S4. Optogenetic inhibition of DLS via activating inhibitory interneurons. **a**, Left: Brain slice illustrating viral expression of mDlx-ChR2-GFP in DLS with an optical fiber track. Scale bar, 0.5 mm. Right: Foxp1 immunostaining (red) marks spiny projection neurons (SPNs), while green indicates ChR2-expressing inhibitory interneurons. Scale bar, 50 μm. **b**, Schematic of microwire array and optic fiber insertion in DLS. Scale bar, 500 μm. **c**, Waveforms of three example ChR2+ units showing optogenetic activation, z-scored. **d**, Rasters for three ChR2+ units. Top: No photo-stimulation; middle: With photo-stimulation; bottom: Spike density functions. Blue shading marks photo-stimulation periods (40 Hz, 5-ms pulse train, 2.2 s duration, coupled to lever press). **e**, Expanded view of stimulation, showing spikes tightly locked to 12 laser pulses (10 repeats shown). **f, g**, Same as **c–d** for five putative SPN units, demonstrating suppressed spiking during photo-stimulation in closed-loop conditions. **h**, Effect of DLS photo-stimulation on 122 putative SPN units (wide waveforms), with z-scored differences in spiking between no-stimulation and photo-stimulation conditions. **i**, Average z-scored differences for the top 60 units from **h**. **j**, Ratio of spike rate in NoStim over Stim conditions plotted against the spike rate during NoStim condition for units with baseline spike rate > 0.5 Hz. A violinplot with a embedded box plot is shown to the right. **k**, Fiber placements and viral expression across 26 rats.

34 **Supplemental Figure 5**

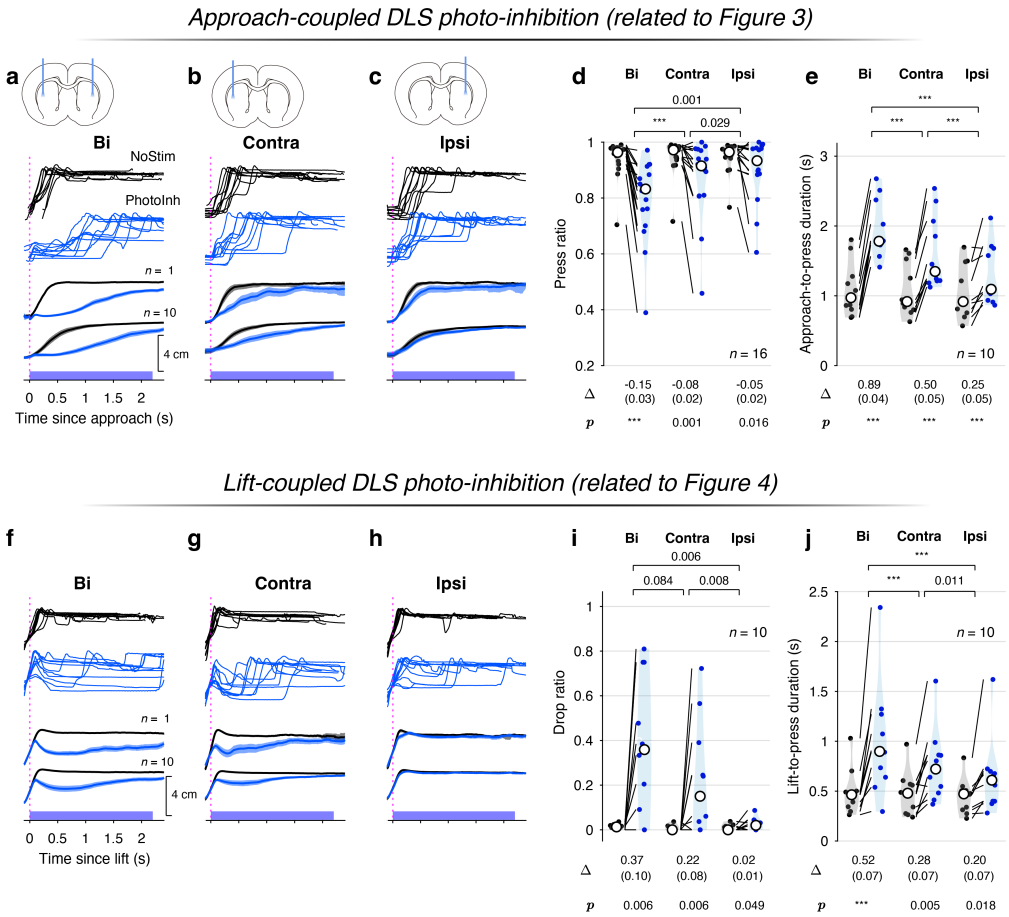

Figure S5. Unilateral versus bilateral DLS photo-inhibition during approach or lift. **a**, Same as Figure 3d (approach-coupled stimulation) for a rat with bilateral (Bi) DLS photo-inhibition ($n=1$) and the average response of all rats ($n=10$). In these rats, both bilateral and unilateral (**b,c**) photo-inhibitions were performed and movement trajectories tracked. For each panel, the first three rows illustrate an example rat (final row: mean and 95% confidence intervals). The fourth row shows the mean and SEM of 10 rats. **b**, Same as **a** for trials in which DLS photo-inhibition was applied to the side contralateral (Contra) to the lifting paw. **c**, Same as **a** for trials in which DLS photo-inhibition was applied to the side ipsilateral (Ipsi) to the lifting paw. **d**, Violin plots display press ratio for no stimulation (NoStim, black) and DLS photo-inhibition (PhotoInh, blue) conditions across bilateral, contralateral, and ipsilateral stimulation sides, with lines connecting paired data from individual rats ($n=16$ rats). Mean changes (PhotoInh$-$NoStim), SEM (in parentheses), and p-values from two-sided Wilcoxon signed-rank tests are listed below each stimulation side. To compare stimulation-induced changes across sides (e.g., Bi vs Contra), a Friedman test was conducted on the (PhotoInh$-$NoStim) differences, treating animals as blocks (Friedman χ^2 = 16.625, d.f. = 2, $p=0.0002$). Post-hoc pairwise Wilcoxon signed-rank tests were applied and Holm-adjusted p-values are shown above the violin plots between pairs of stimulation sides. $***$ denotes $p<0.001$. **e**, Violin plots display approach-to-press duration (t_{a2p}) distributions (see Equation 7). **f–h**, Same as Figure 4d (lift-coupled stimulation) for a rat with bilateral (Bi) DLS photo-inhibition ($n=1$) and the average response of 10 rats ($n=10$) for which both bilateral (**f**) and unilateral (**g,h**) photo-inhibitions were performed. **i**, Same as **d** for drop rate when DLS photo-inhibition was applied during lifting. To compare the effect across different stimulation sides, the Friedman test was conducted (Friedman χ^2 = 16.2, d.f. = 2, $p=0.0003$). **j**, Same as **e** for lift-to-press duration (t_{l2p} (Equation 11).

Supplemental Figure 6

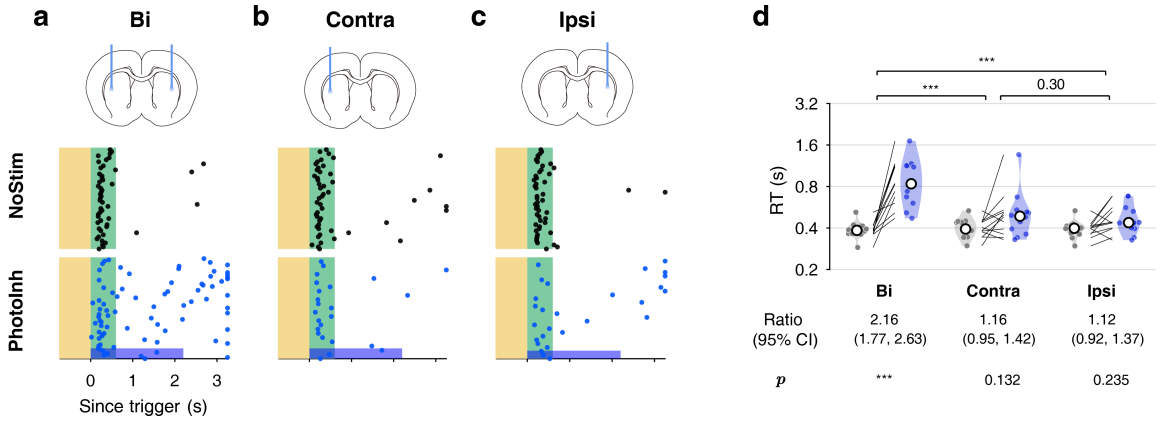

Figure S6. Unilateral versus bilateral DLS photo-inhibition coupled to trigger stimulus. **a–c**, Lever-release responses in an example rat during bilateral (Bi, **a**), contralateral (Contra, **b**), and ipsilateral (Ipsi, **c**) DLS photo-inhibition. Top row, NoStim; bottom row: PhotoInh. **d**, Geometric mean reaction time (RT) ratios (PhotoInh/NoStim) across rats under Bi, Contra, and Ipsi conditions. Data were analyzed using a LME model on log-transformed RTs (log(RT) $\sim$ StimType × StimSide + (1 + StimType | anm)), where StimType (PhotoInh or NoStim) and StimSide (Bi, Contra, or Ipsi) are fixed effects. EMMs were computed for each combination, followed by post-hoc contrasts testing the log(RT) differences (PhotoInh—NoStim) within each StimSide and across StimSides (Bi - Contra, Bi - Ipsi, Contra - Ipsi), with Holm-adjusted p-values. Ratios and 95% confidence intervals are exponentiated to the original RT scale; $***$ denotes $p < 0.001$.

Supplemental Figure 7

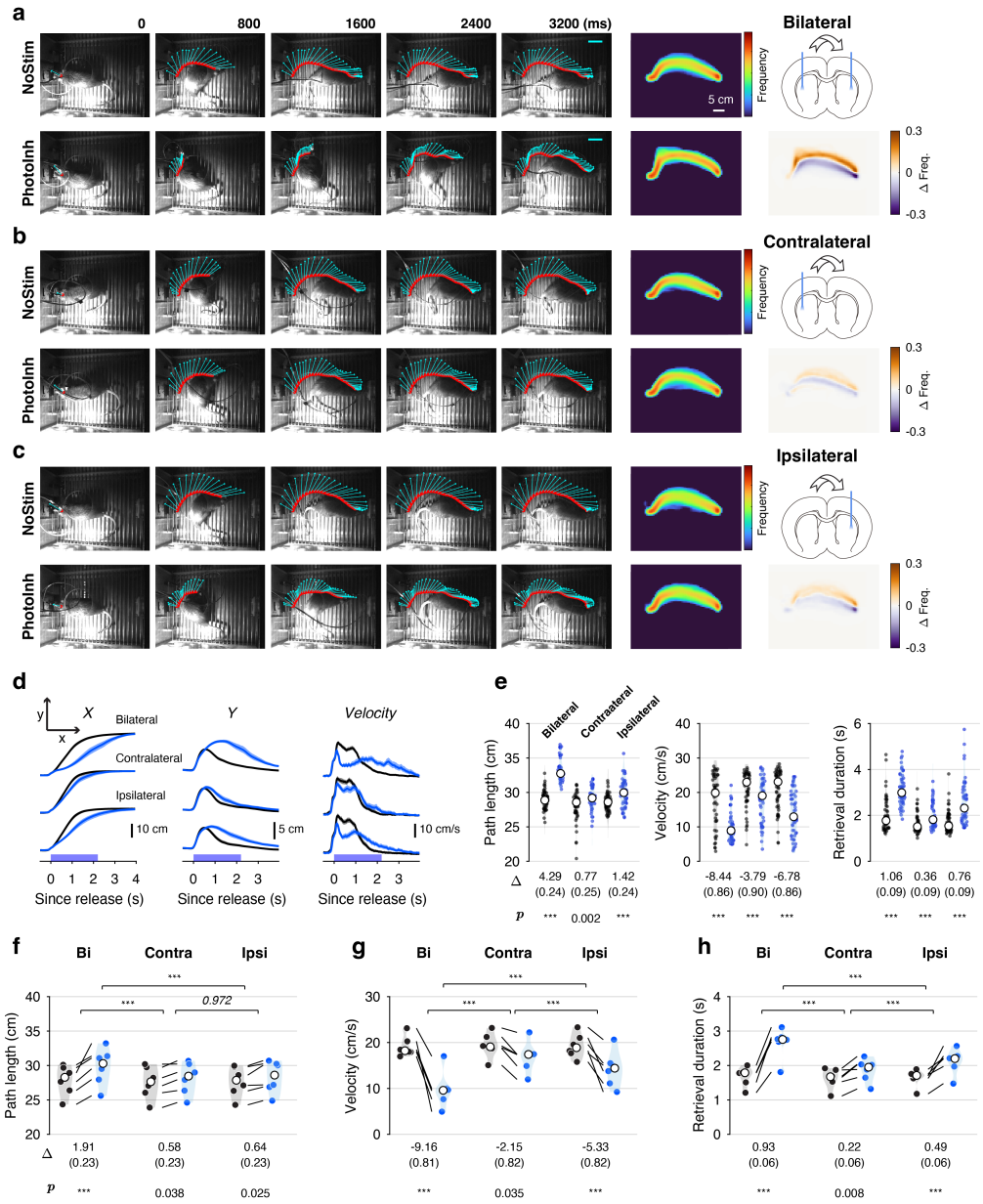

Figure S7. Unilateral versus bilateral DLS photo-inhibition during reward retrieval. **a**, Movement trajectories and frequency map differences for bilateral photo-inhibition. Arrows above coronal brain sections indicate turning direction toward the reward port post-lever release; fiber locations show photo-inhibition sites. Color maps indicate pixel traversal frequency differences (PhotoInh−NoStim). **b**, As in **a** for contralateral photo-inhibition. **c**, As in **a** for ipsilateral photo-inhibition. **d**, Mean movement in X and Y dimensions and instantaneous velocity with 95% confidence intervals across stimulation sides (bilateral, ipsilateral, contralateral) for a representative rat. **e**, Movement path length, mean velocity, and retrieval duration for the representative rat; mean differences (SEM in parentheses) and Holm-adjusted p-values from a linear model shown below. **f–h**, As in **e** for $n=6$ rats; Holm-adjusted p-values are from post-hoc pairwise contrasts based on EMMs from the LME model; $***$ denotes $p<0.001$.

Supplemental Figure 8

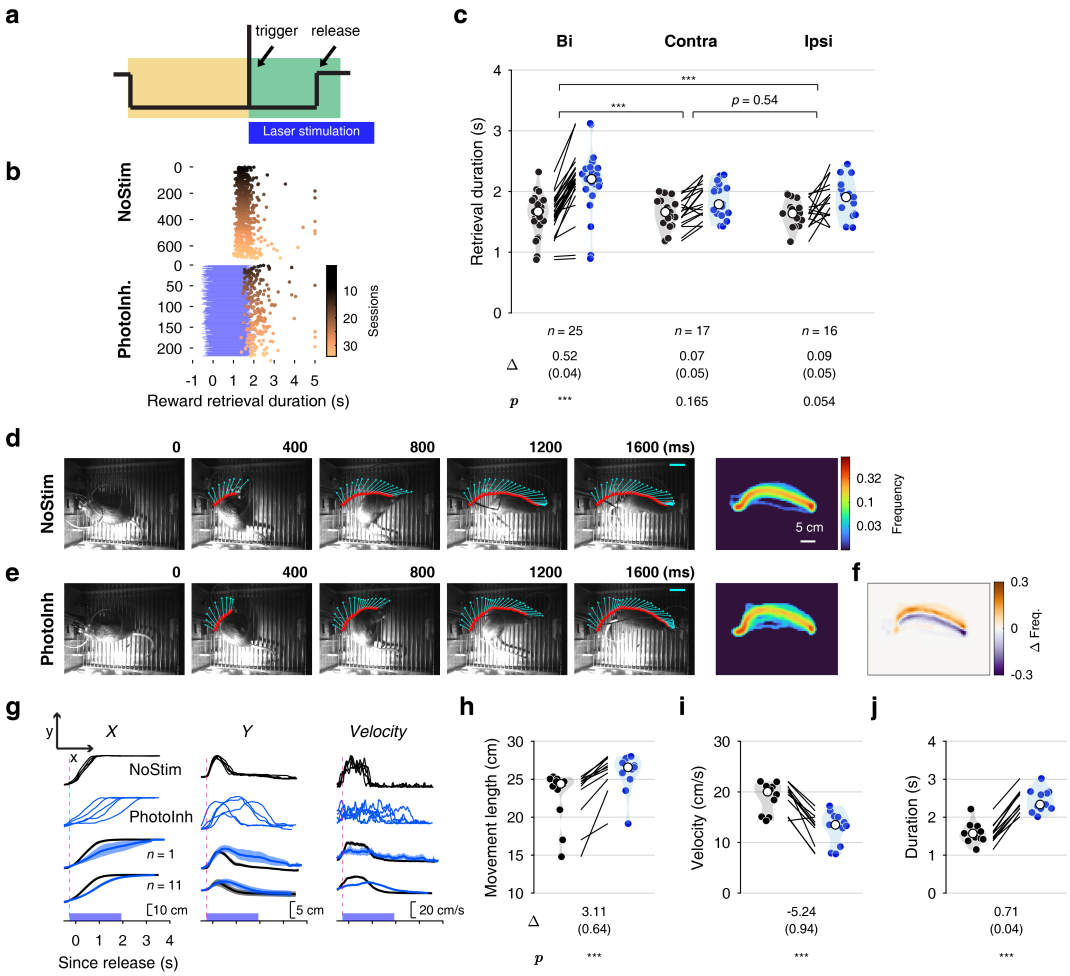

Figure S8. Trigger-coupled DLS photo-inhibition slows down reward retrieval and locomotion. a. Schematic of trigger-coupled DLS photo-inhibition. **b.** Reward retrieval duration with and without bilateral photo-inhibition (25% of trials) in a representative rat. Each dot represents duration to reach the reward port after lever release (time = 0); blue shading indicates photo-inhibition duration. **c.** Mean differences in retrieval duration (SEM in parentheses) for bilateral or unilateral photo-inhibition; Holm-adjusted p-values are from post-hoc pairwise contrasts based on EMMs from a LME model (duration $\sim$ StimType × StimSide + (1 + StimType | anm)). **d–f.** As in Figure 6c–e for photo-inhibition starting at trigger stimulus onset; time 0 denotes lever release. **g.** Movement in X and Y dimensions and instantaneous velocity; blue rectangles indicate photo-inhibition period aligned to trigger onset. **h–j.** Mean movement path length, mean velocity, and retrieval duration in $n = 11$ rats; Holm-adjusted p-values are from post-hoc pairwise contrasts based on EMMs from a LME model; $***$ indicates $p < 0.001$.

38 **Supplemental Figure 9**

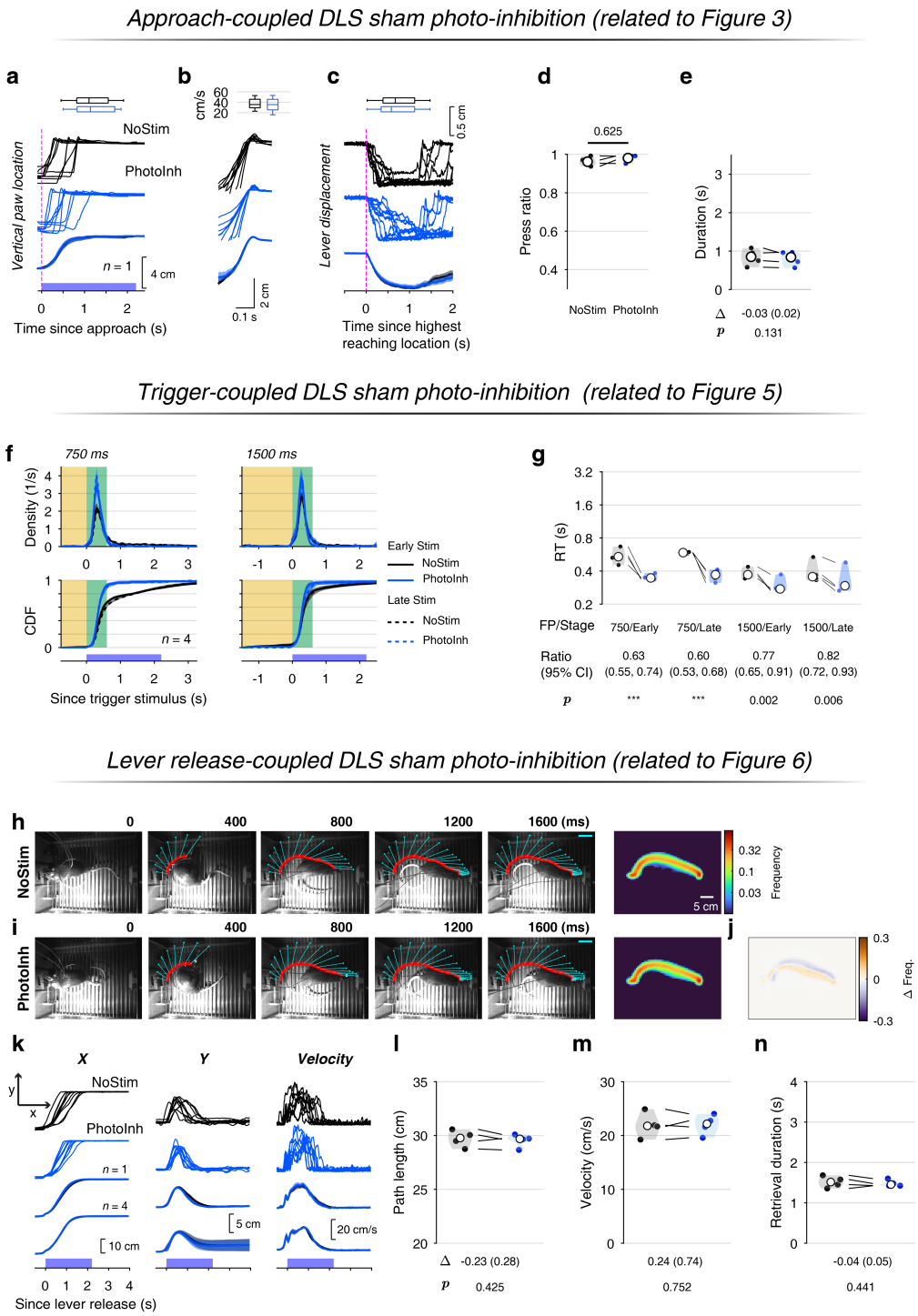

Figure S9. Control experiments. **a–e**, As in Figure 3d–h but for control group ($n = 4$ rats) expressing mDlx-GFP (instead of mDlx-ChR2-GFP) in the DLS. Experiments (DLS photo-stimulation was coupled to lever approach) and statistical analyses (with LME) matched the photo-inhibition group. **f–g**, As in Figure 5c,d for control rats. DLS photo-stimulation was coupled to trigger stimulus. **h–n**, As in Figure 6c–i for control rats. DLS photo-stimulation was coupled to lever release.

Supplemental Figure 10

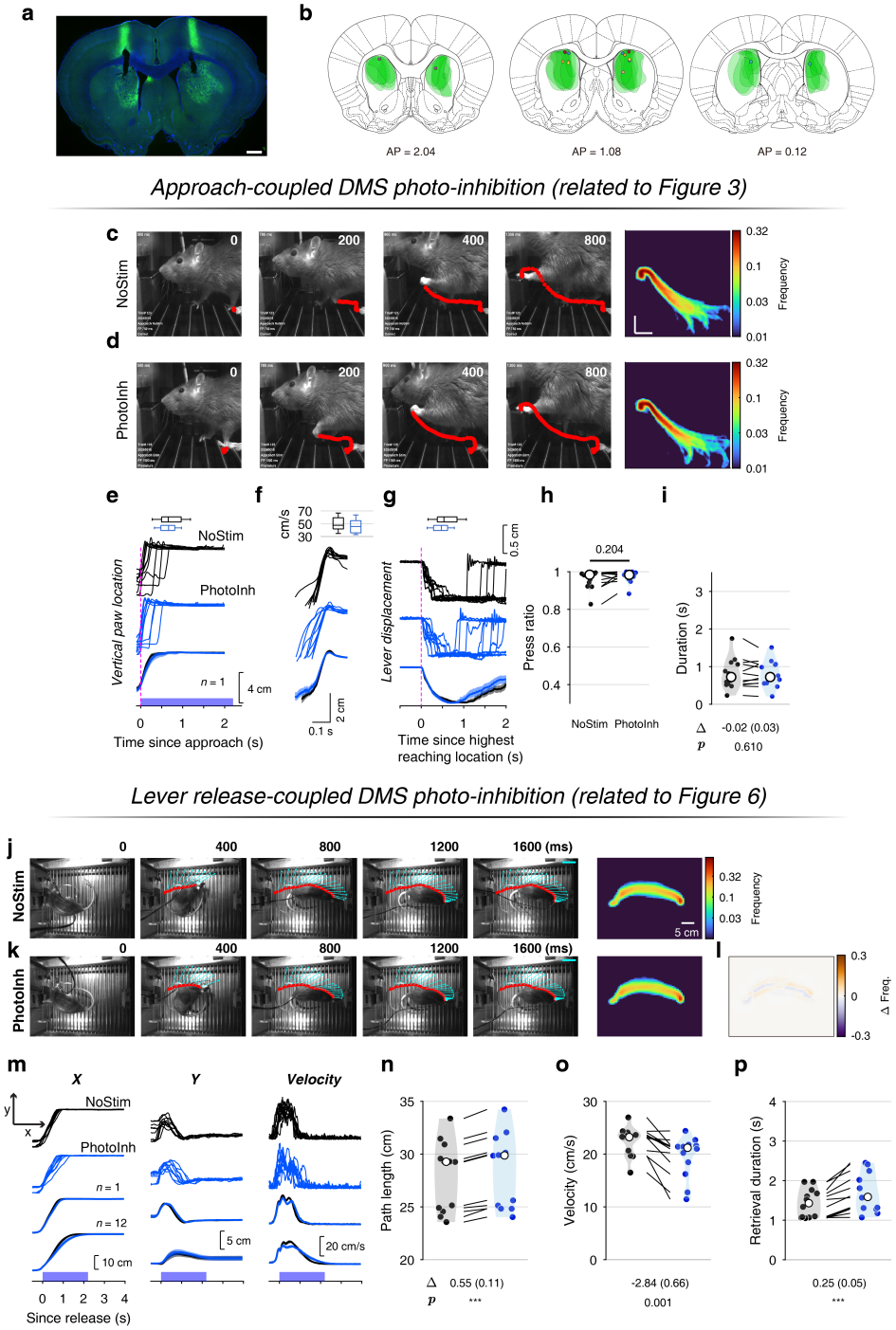

Figure S10. Bilateral DMS photo-inhibition during approach or reward retrieval. a, Brain slice illustrating viral expression of mDlx-ChR2-GFP in the DMS with an optical fiber track. Scale bar, 1 mm. **b**, Fiber placements and viral expression in 8 rats. **c–i**, As in Figure 3b–h but for DMS photo-inhibition rats ($n = 12$) with mDlx-ChR2-GFP expressed in inhibitory interneurons of the DMS. Experiments (DMS photo-inhibition was coupled to lever approach) and statistical analyses were conducted as in the DLS photo-inhibition group. **j–p**, As in Figure 6c–i, with DMS photo-inhibition coupled to lever release.

Supplemental Figure 11

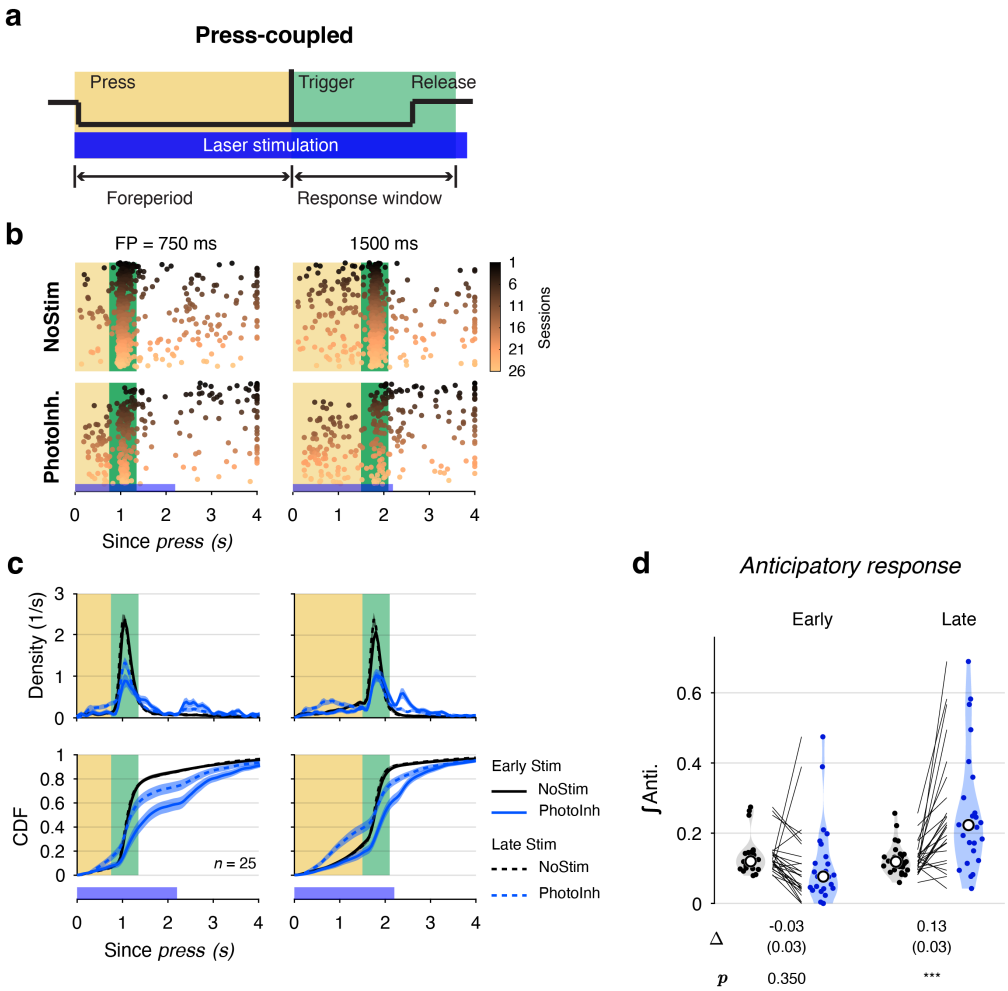

Figure S11. Press-coupled DLS photo-inhibition increases anticipatory responses. a–c, Similar to Figure 5a–c, but for DLS photo-inhibition coupled to lever press and holding. **d**, Integral of anticipation function with (blue) or without (gray) photo-inhibition across $n=25$ rats, grouped by photo-inhibition history (Early, Late). Mean differences (PhotoInh minus NoStim), SE, and Holm-adjusted p-values from pairwise EMM contrasts are displayed below.

The anticipation function $G(t)$ for premature responses was computed on 10-ms intervals from $t=0$ to 1.5 s; the denominator of $G(t)$ represents the number of trials with FP equals to or longer than the interval, and the numerator is the cumulative count of premature responses up to that interval:

$$\begin{aligned} G(t) &= \frac{N_1 \cdot F_1(t) + N_2 \cdot F_2(t)}{N_1 + N_2}, \quad && \text{for } t < 0.75 \\ &= \frac{N_2 \cdot F_2(t)}{N_2}, && \text{for } 0.75 \leq t < 1.5 \end{aligned} \tag{1}$$

where N_i $(i=1,2)$ is the number of trials with FPs = 0.75 s and 1.5 s. $F_i(t)$ $(i=1,2)$ is the fraction of premature responses at or before time t.

The integral (y) of $G(t)$ from 0 to 1.5 s quantified premature response magnitude and was analyzed using an LME model to examine the effect of photo-inhibition on waiting ($y \sim \text{StimType} \times \text{StimStage} + (1 + \text{StimType} \mid \text{anm})$):

$$\begin{aligned} y_{js} = \beta_0 + \beta_1 \, \text{StimType}_{js} + \beta_2 \, \text{StimStage}_{js} + \beta_3 \left(\text{StimType}_{js} \times \text{StimStage}_{js}\right) \\ + u_{0j} + u_{1j} \, \text{StimType}_{js} + \varepsilon_{js} \end{aligned} \tag{2}$$

where y_{js} is the integral value of the anticipation function for StimStage s (Early or Late) in animal j.

Supplemental Figure 12

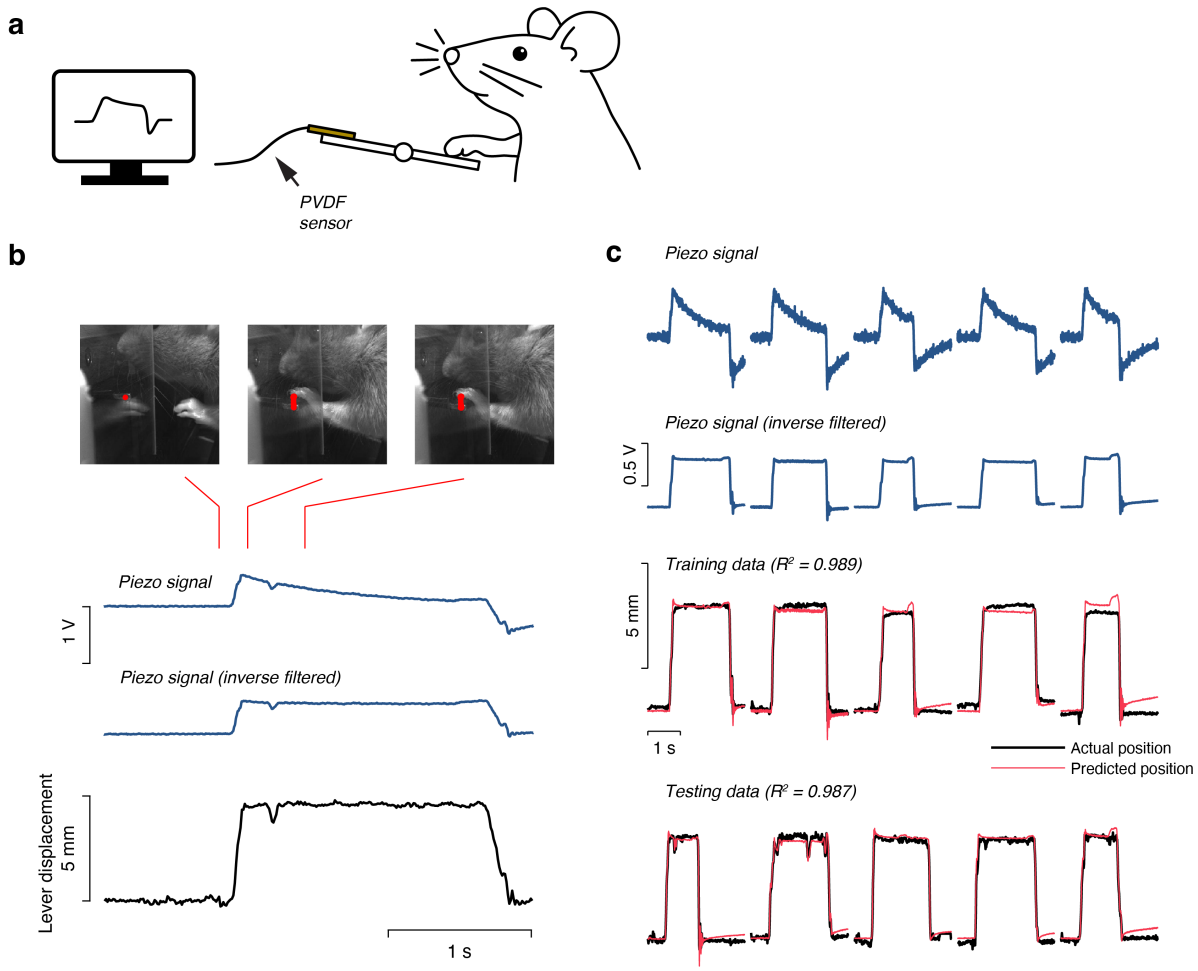

Figure S12. Piezo-sensor signal mapping to lever position. **a**, Diagram of a piezoelectric (PVDF) sensor attached to the opposite end of the lever to detect lever motion. **b**, Comparison of piezo-sensor signal and lever position during a lever press. The sensor signal, low-pass filtered during acquisition, was reconstructed via inverse filtering; lever position was tracked from video. **c**, Reconstructed piezo signal predicts lever position with a linear model, enabling rapid and accurate lever-position estimation.

Supplemental Video 1

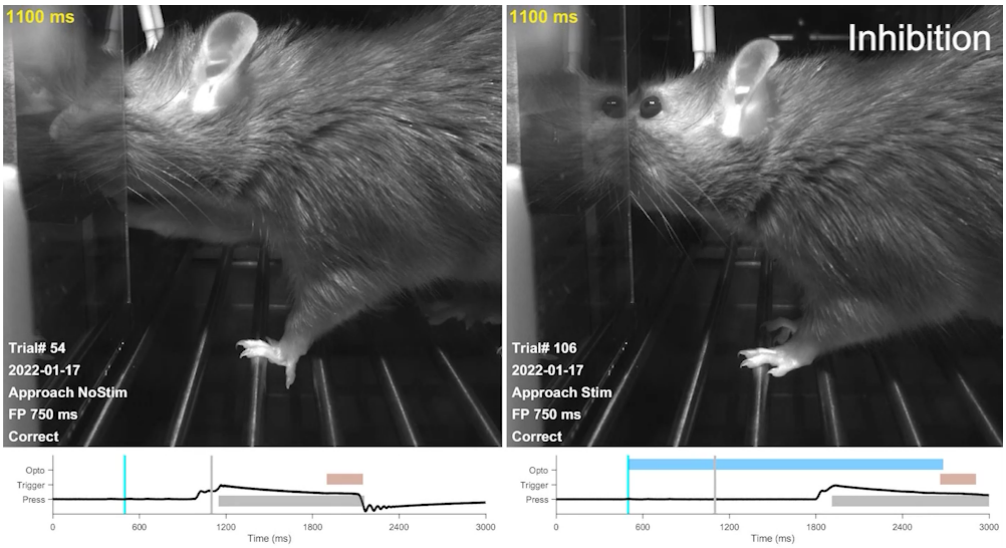

Video S1. Comparison of forelimb reaching in a no-stimulation trial (left) and an approach-coupled DLS photo-inhibition trial (right). The video plays at $0.1\times$ real-time speed (tenfold slower). The bottom panel shows the piezo-sensor signal. Blue, brown, and gray shading indicate the duration of laser stimulation, trigger stimulus, and holding period. A cyan vertical line marks the approach detection in both panels. A gray vertical line marks the time of the current frame.

Supplemental Video 2

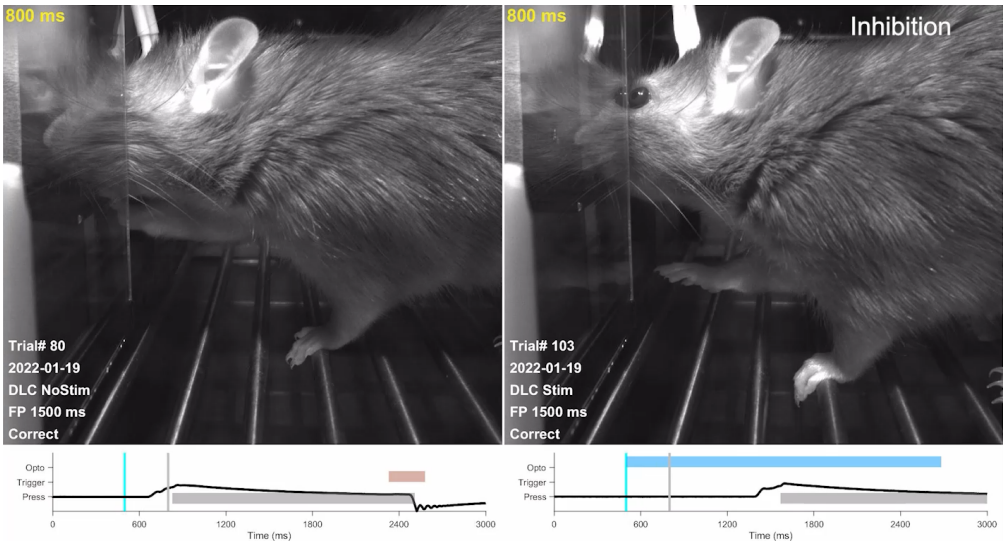

Video S2. Comparison of forelimb reaching in a no-stimulation trial (left) and a lift-coupled DLS photo-inhibition trial (right). The video plays at 0.1× real-time speed (tenfold slower). Panels match Video S1; the bottom panel shows the piezo-sensor signal. Blue, brown, and gray shading denote the laser-stimulation period, the trigger stimulus, and the holding period, respectively. A cyan line marks paw-lift detection; a gray vertical line marks the time of the current frame.

Supplemental Video 3

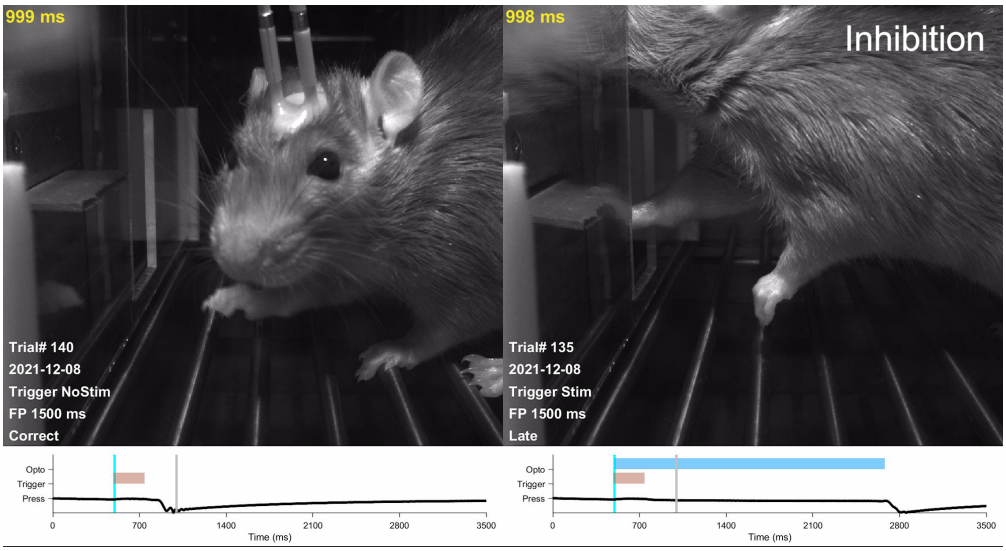

Video S3. Comparison of lever release in a no-stimulation trial (left) and a trigger-coupled DLS photo-inhibition trial (right). The video plays at $0.1\times$ real-time speed (tenfold slower). Panels match Video S1; the bottom panel shows the piezo-sensor signal. Blue, brown, and gray shading denote the laser-stimulation period, the trigger stimulus, and the holding period, respectively. A cyan line marks the trigger stimulus in both panels. A gray vertical line marks the time of the current frame.

Supplemental Video 4

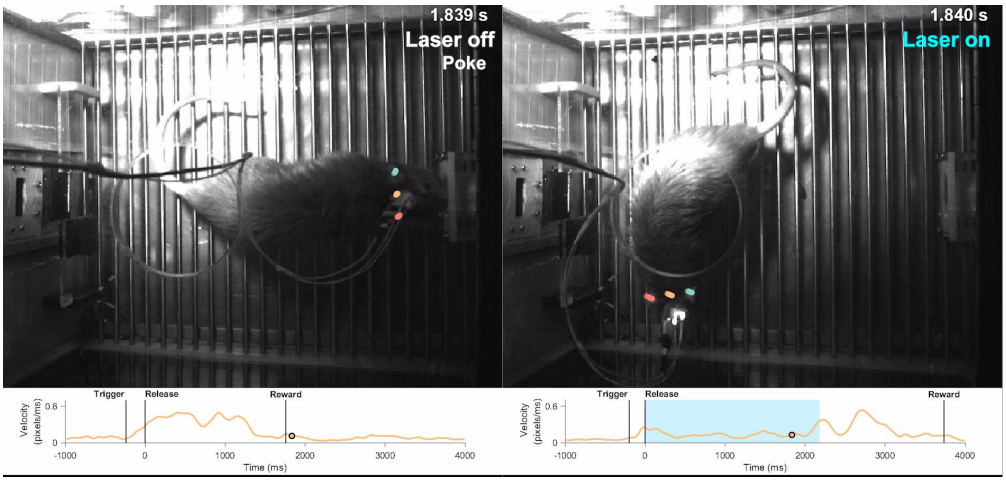

Video S4. Comparison of reward retrieval in a no-stimulation trial (left) and a release-coupled DLS photo-inhibition trial (right). The video plays at $0.2\times$ real-time speed (fivefold slower). Tracking markers: red, right ear; green, left ear; yellow, midpoint between ears. The bottom panel shows the velocity of the midpoint. A circle tracks the time of the current frame.

Supplemental Video 5

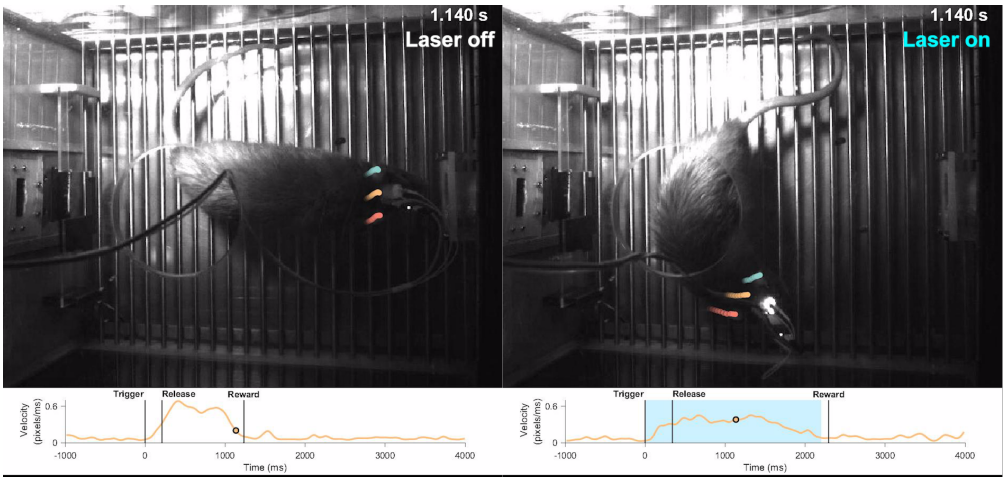

Video S5. Comparison of reward retrieval in a no-stimulation trial (left) and a trigger-coupled DLS photo-inhibition trial (right). The video plays at $0.2\times$ real-time speed (fivefold slower). Tracking markers: red, right ear; green, left ear; yellow, midpoint between ears. The bottom panel shows the velocity of the midpoint. A circle tracks the time of the current frame.

Supplemental Video 6

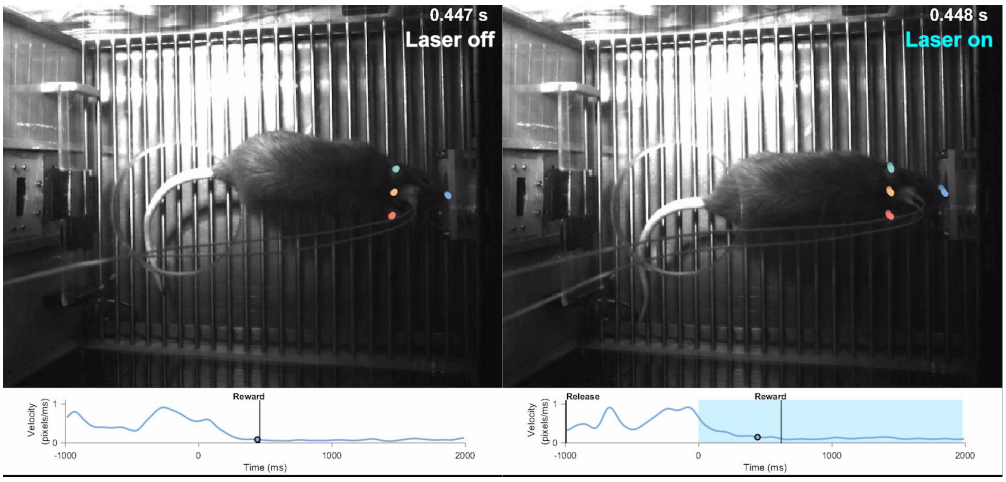

Video S6. Comparison of reward retrieval in a no-stimulation trial (left) and a poke-coupled DLS photo-inhibition trial (right). The video plays at $0.2\times$ real-time speed (fivefold slower). Tracking markers: red, right ear; green, left ear; yellow, midpoint between ears; blue, nose. The bottom panel shows the velocity of the nose. A circle tracks the time of the current frame.